

¹ Modeling ice shelf cavities and calving tabular
² icebergs

A.A. Stern,¹, A. Adcroft¹ and O. Sergienko¹, G. Marquez¹, R. Hallberg¹

³ **Key Points:**

⁴

A. A. Stern, Geophysical Fluid Dynamics Laboratory, Princeton University

A. Adcroft, Geophysical Fluid Dynamics Laboratory, Princeton University

O. Sergienko, Geophysical Fluid Dynamics Laboratory, Princeton University

G. Marquez, Geophysical Fluid Dynamics Laboratory, Princeton University

R. Hallberg, Geophysical Fluid Dynamics Laboratory, Princeton University

5 **Abstract.** The calving of giant icebergs is an important process in the
6 Antarctic freshwater cycle. Iceberg calving can significantly alter the geom-
7 etry of an ice shelf cavity, potentially affecting the circulation within the cav-
8 ity. Furthermore, giant icebergs which break away can drift across large dis-
9 tance, altering ocean circulation, sea ice distributions and bottom water for-
10 mation. However despite its importance, the current generation of nu-
11 merical models is unable to represent this process in a physically realistic way.
12 In this study we develop a model of an ice shelf cavity using a Lagrangian
13 ice shelf. The ice shelf is constructed out of Lagrangian elements which are
14 bonded together by numerical bonds. This Lagrangian framework allows for
15 large pieces of the ice shelf to break away and become tabular icebergs. The
16 model developed in the manuscript is referred to as the Lagrangian Iceberg/Ice
17 Shelf Model (LIISM). This paper provides a description of the LIISM model
18 and discusses a number of the technical elements involved in building a La-
19 grangian ice shelf. To test the model, the LIISM is used to model an ideal-
20 ized ice shelf cavity which was developed as part of the Marine Ice Ocean
21 Modeling Inter-comparison Project (MISOMIP). Results from static ice shelf
22 experiments compare well to results using a more traditional Eulerian ice
23 shelf cavity. The novel capabilities of the LIISM are demonstrated by mod-
24 eling a tabular iceberg breaking away from the idealized ice shelf.

1. Introduction

Floating ice shelves cover vast regions of the Antarctic polar oceans. These massive platforms of ice extend deep into the water column, applying large pressures to surface of the ocean, which is often hundreds of meters below global sea level. Beneath the ice shelves, both the bottom topography and the ice shelf geometry play a role in steering ocean currents [Nicholls , 1996; Jenkins et al , 2010; Stern et al , 2014]. The topographic constraint imposed by the ice shelf at the ocean's upper boundary significantly affects the circulation within the ice shelf cavities, and gives the ocean within the ice shelves cavities a unique character.

In addition to suppressing the depth of ocean surface, the ice shelves also melt (and break), thus providing a freshwater flux into the ice shelf cavities. Ice shelf melting and breaking are key components in the Antarctic meltwater system, and affect the ocean hydrography and biology both inside and outside of the ice shelf cavities. Some elements of the this Antarctic meltwater system are discussed in the following paragraphs.

Within the ice shelf cavities, the input of buoyant meltwater into the ocean creates rising density plumes, which are guided along the ice shelf base, and help drive ocean circulation beneath the ice shelves [MacAyeal , 1984; Holland and Feltham , 2006]. The strength of the circulation within the cavity feeds back onto the ice shelf melt rates, by removing cold water from the cavity, and drawing in warmer waters from the open ocean, thus providing the constant supply of thermal energy needed for continuous ice shelf melt [Lewis and Perkin , 1986; Jacobs et al , 2011].

45 The Antarctic ice shelves are also characterized by large infrequent calving events where
46 massive pieces of the ice shelves break off, to create giant tabular icebergs. Observational
47 estimates suggest that approximately half of Antarctic ice shelf decay is due to iceberg
48 calving, while the other half occurs through ice shelf melting [Depoorter et al , 2013;
49 Rignot et al , 2013]. Calving icebergs' sizes appear to fit a power law distribution, with
50 the majority of icebergs being small ($L < 1$ km), while giant tabular icebergs ($L > 5$ km)
51 account for more than 90% of the icebergs mass [Tournadre et al , 2016]. After calving,
52 icebergs slowly drift away from their mother glaciers, often becoming stuck in sea ice, or
53 become grounded along the Antarctic coast [Lichey and Hellmer , 2001; Dowdeswell and
54 Bamber , 2007]. Giant tabular icebergs also extend deep into the water column, and have
55 to potential to disrupt ocean circulation patterns for months or even years after calving
56 [Robinson et al , 2012; Stern et al , 2015].

57 Melt water from both ice shelf melt and iceberg melt impact the ocean hydrography
58 outside of the ice shelf cavities, influencing sea ice production and bottom water formation
59 [Arrigo et al , 2002; Robinson et al , 2012; Nicholls et al , 2009]. The long distances traveled
60 by giant icebergs before melting means that their meltwater impact is often felt hundreds
61 of kilometers away from their calving origins [Stern et al , 2016]. Melt water injection (and
62 the accompanying upwelling) from ice shelves and icebergs can also influence biological
63 productivity by providing nutrients to the surface ocean or changing sea ice conditions
64 [Arrigo et al , 2002; Vernet et al , 2012; Biddle et al , 2015]. The increased productivity
65 associated with free floating tabular icebergs has been linked with local increases in ocean
66 carbon uptake, potentially large enough to be a significant fraction of the Southern Ocean
67 carbon sequestration [Smith et al , 2007].

68 In recent years society's need for improved projections of future sea level has lead to an
69 increased focus on the Antarctic meltwater system described in the previous paragraphs.
70 This increased interest has led to accelerated efforts to accurately model Antarctic ice shelf
71 cavities [Asay-Davis et al , 2016]. Modeling the ocean beneath the ice shelves presents
72 a unique set of challenges, since (i) the presence of ice shelves provides a rigid upper
73 boundary for the ocean model which is not encountered elsewhere in the ocean, and
74 (ii) melting and breaking ice shelves imply a changing ocean boundary conditions which
75 present numerous numerical difficulties.

76 The earliest models of ocean ice shelf cavities were developed using a static ice shelf
77 with a fixed shape [Hellmer and Olbers , 1989; Determan and Gerdes , 1994; Grosfeld et
78 al , 1997; Holland and Jenkins , 2001; Losch , 2008]. In these models, ice shelf melting
79 was represented through salinity and temperature fluxes, while the ice shelf geometry
80 remained unchanged. Later models of ice shelf cavities allowed the ice shelf geometry
81 to evolve as the ice shelf melted, permitting the study of coupled ocean-ice phenomena
82 [Gladish et al , 2012; Sergienko , 2013]. More recently, dynamic ice shelf models have
83 been coupled the ocean cavity, allowing the study of grounding line migration, which is of
84 key importance for sea level rise projections [Grosfeld and Sandhger , 2004; Goldberg et
85 al , 2012; De Rydt and Gudmundsson , 2016]. As far as we know, all models of ice shelf
86 cavities to date have neglected ice shelf breaking and iceberg detachment.

87 In parallel to these efforts to develop ice shelf cavity models, a number of iceberg drift
88 models have been developed, and have been included in some global General Circulation
89 Models [Bigg et al , 1997; Gladstone et al , 2001; Martin and Adcroft , 2010; Marsh et al ,
90 2015]. These iceberg drift models treat icebergs as Lagrangian point particles, which are

adverted by the flow, and melt according to certain parameterizations for icebergs melt.

Since icebergs are treated as point particles, the iceberg drift models are mostly suitable for modeling smaller icebergs drifting across large distances, and as such iceberg drift models have mostly been used to represent icebergs smaller than 3.5km on a global scale [Jongma et al , 2009; Martin and Adcroft , 2010; Marsh et al , 2015]. These models are not suitable for modeling larger tabular icebergs, which feel the ocean over many grid cells, depress the ocean surface and change circulation patterns [Stern et al , 2016]. They also not suitable for studying the local effects that icebergs have on the surrounding ocean. For this reason, tabular icebergs ($L > 5\text{km}$) are currently not represented in the iceberg drift models used in climate models, even though observations suggest that tabular icebergs account for the vast majority of the total Southern Hemisphere icebergs mass [Tournadre et al , 2016].

The ice shelf cavity models and iceberg drift models described above have been developed separately from one another, and have not been designed to be used together in a physically consistent way. As such, it has not been possible to model the calving of tabular icebergs away from an ice shelf, which is an important part of the Antarctic climate system. The goal of this study is to develop a model which combines features of the ice shelf cavity models and the iceberg drift models, to create an ice shelf cavity model that is able to calve tabular icebergs. To do this, we create an ice shelf model out of Lagrangian elements which are ‘bonded’ together by numerical bonds. In this framework, icebergs do not get created when a calving event takes place (as in iceberg drift models), but rather the icebergs ‘break’ away from an existing ice shelf, thus changing the geometry of the ice shelf cavity. Modeling iceberg calving in a physically consistent way allows us

¹¹⁴ to study the ocean response to iceberg detachment (see Figures ?? and Figures ??, for
¹¹⁵ example). Also, by allowing icebergs protrude deep into the water column we can study
¹¹⁶ the ocean dynamics around individual tabular icebergs (which was not possible in iceberg
¹¹⁷ drift models).

¹¹⁸ In all simulation in this study, the shape of the calving iceberg is prescribed. The
¹¹⁹ question of how to correctly prescribe a calving law is undoubtably a very important
¹²⁰ question, which has rightfully received much attention in recent years [Benn et all , 2007;
¹²¹ Alley et al , 2008; Levermann et al , 2012]. Bassis and Jacobs [2013], for example, used
¹²² a DEM model to study the generation and propagation of cracks within an ice shelf (not
¹²³ coupled to a dynamic ocean model). In this study, we bypass the question of how to
¹²⁴ correctly calve icebergs or break bonds. Instead we focus on developing a framework to
¹²⁵ model the ocean to response to ice shelf breaking and the presence of tabular icebergs.
¹²⁶ This framework of representing ice shelves using a Lagrangian grid might be a step towards
¹²⁷ including giant tabular icebergs in climate models. Including ice fracture into this model
¹²⁸ will be a later step.

¹²⁹ The model developed in this study is referred to at the Lagrangian Iceberg/Ice Shelf
¹³⁰ Model (LIISM). Section 2 gives a description of many of the key aspects of the LIISM.
¹³¹ Since this model is a new approach to modeling ice shelf cavities, we present many of
¹³² the technical elements involved in constructing the model. Those readers who are more
¹³³ interested in the model capabilities, should skip directly to the model results in the later
¹³⁴ sections. In Section 3 and 4, the LIISM model is used to simulate the circulation beneath
¹³⁵ an idealized ice shelf. The LIISM model results are validated by comparing them to an
¹³⁶ existing ice shelf model. We then we move beyond the capabilities of the existing ice shelf

₁₃₇ model by allowing a piece of the ice shelf to break away becoming a tabular icebergs, and
₁₃₈ consider the ocean response to this calving event.

2. Model description

₁₃₉ In this section we describe many key elements of the LIISM. The LIISM is a
₁₄₀ Lagrangian/particle-based model in that the objects of the model are Lagrangian ele-
₁₄₁ ments. Each element represents a mass of ice which is floating in the ocean, and has a
₁₄₂ position, velocity, mass, and a set of dimensions, which can evolve in time. The motion of
₁₄₃ each element is determined by a momentum equation which is solved in the (Lagrangian)
₁₄₄ reference frame of the element. The elements are forced by oceanic and atmospheric
₁₄₅ forces, which are provided by the user or are determined by coupling the LIISM to an
₁₄₆ ocean/atmosphere model. The elements also interact with one another and can be bonded
₁₄₇ together to form larger structures. In different contexts, the LIISM elements can be
₁₄₈ thought to represent individual icebergs, sea ice flows, or, when the elements are bonded
₁₄₉ together, they can represent larger structures such as tabular icebergs or ice shelves. In
₁₅₀ this latter case, the LIISM model can be categorized as a discrete element model (DEM).

₁₅₁ The LIISM model is developed on the code base of an existing iceberg drift model
₁₅₂ [Martin and Adcroft , 2010; Stern et al , 2016]. When run with the correct set of runtime
₁₅₃ flags, the model runs as a traditional iceberg drift model.

2.1. Equations of motion

₁₅₄ The elements drift in the ocean, forced by atmosphere, ocean and sea-ice drag forces,
₁₅₅ as well as the Coriolis force and a force due to the sea surface slope. When these ice
₁₅₆ elements move alone (without interactions with other elements), they can be thought of

¹⁵⁷ as representation of small icebergs, and follow the same equations described in the iceberg
¹⁵⁸ drift model of Martin and Adcroft [2010] (based on the equations outlined in Bigg et al
¹⁵⁹ [1997]; Gladstone et al [2001]).

¹⁶⁰ In addition to the environmental forces, the elements in the LIISM model experience
¹⁶¹ interactive forces due to the presence of other elements. Two types of interactive forces are
¹⁶² included between elements. The first force is repulsive force which is applied to elements
¹⁶³ to prevent them from moving too close to one another. This repulsive force prevents
¹⁶⁴ icebergs from piling up on top of one another. The second interactive force is a force due
¹⁶⁵ to numerical ‘bonds’, and is only applied if two elements are ‘bonded’ together. When
¹⁶⁶ two elements are bonded, each element feels an attractive force that prevents the elements
¹⁶⁷ from moving too far apart from one another. The interactive forces between two bonded
¹⁶⁸ elements are defined such that in the absence of other forces the elements come to rest
¹⁶⁹ adjacent to one another, with no overlap of the iceberg areas.

The momentum equation for each element is given by

$$M \frac{D\vec{u}}{Dt} = \vec{F}_A + \vec{F}_W + \vec{F}_R + \vec{F}_C + \vec{F}_{SS} + \vec{F}_{SI} + \vec{F}_{IA}, \quad (1)$$

¹⁷⁰ where $\frac{D}{Dt}$ is the total (Lagrangian) derivative, M is the mass of the element, \vec{u} is the
¹⁷¹ velocity of the element, and the terms on the right hand side give the forces on the
¹⁷² element due to air drag (\vec{F}_A), water drag (\vec{F}_W), sea ice drag (\vec{F}_{SI}), Coriolis force (\vec{F}_C),
¹⁷³ wave radiation force (\vec{F}_R), sea surface slope (\vec{F}_{SS}), and interactions with other elements
¹⁷⁴ (\vec{F}_{IA}). The environmental forces are the same as those presented in Martin and Adcroft
¹⁷⁵ [2010], and are provided for completeness in Appendix A. The details of the interactive
¹⁷⁶ forces are provided in below.

2.2. Interactive Forces

The interactive force on an element is calculated by adding together the interactions with all other elements, such that the interactive force on element i , $(\vec{F}_{IA})_i$ is given by:

$$(F_{IA})_i = \sum_{j \neq i} (F_{IA})_{ij}, \quad (2)$$

where $(F_{IA})_{ij}$ is the force on element i by element j . Both bonded and repulsive interactions are modeled using elastic stresses with frictional damping. The elastic component of the force is a function of the distance between the two elements, while the frictional damping force depends on the relative velocity of the two elements.

To describe the forces between two elements, we begin by introducing some notation.

Let \vec{x}_i , \vec{x}_j be the positions of elements i and j . The distance between elements i and j is

$$d_{ij} = |\vec{x}_i - \vec{x}_j|. \quad (3)$$

We then define the interaction diameter of an element by

$$D_i = 2\sqrt{\frac{A_i}{\pi}}, \quad (4)$$

where A_i is the planar surface area of element i . Using this, we define the critical interactive length scale,

$$L_{ij} = \frac{D_i + D_j}{2}, \quad (5)$$

which governs interactions between elements i and j . Repulsive forces are only applied when $d_{i,j} < L_{i,j}$, while bonded forces are only applied when $d_{i,j} > L_{i,j}$ and a bond exists between element i and j . Bond and repulsive forces are designed to such that in the absence of other forces, bonded particles will settle in an equilibrium position where elements are separated by the critical interaction length scale $L_{i,j}$.

To aid in notation, we define a bond matrix B_{ij} such that $B_{ij} = 1$ if elements i and j are bonded together and $B_{ij} = 0$ otherwise. Using this notation, the interactive force $(\vec{F}_{IA})_{ij}$ on an element i by an element j is given by

$$(\vec{F}_{IA})_{ij} = \begin{cases} (\vec{F}_e)_{ij} + (\vec{F}_d)_{ij} & \text{if } d_{ij} \leq L_{ij} \\ (\vec{F}_e)_{ij} + (\vec{F}_d)_{ij} & \text{if } d_{ij} > L_{ij} \text{ and } B_{ij} = 1 \\ 0 & \text{if } d_{ij} > L_{ij} \text{ and } B_{ij} = 0 . \end{cases} \quad (6)$$

$(\vec{F}_e)_{ij}$ and $(\vec{F}_d)_{ij}$ are the elastic and frictional damping components of the interactive force between elements i and j. The elastic force $(\vec{F}_e)_{ij}$ between elements is given by

$$(\vec{F}_e)_{ij} = -\kappa_e \left(d_{i,j} - L_{i,j} \right) T_{i,j} \vec{r}, \quad (7)$$

where $\vec{r} = \frac{(\vec{x}_i - \vec{x}_j)}{|\vec{x}_i - \vec{x}_j|}$ is the directional unit vector between the position of element i and j, and κ_e is the spring constant, and $T_{i,j}$ is the minimum of the thickness of elements i, j.

We choose $(\vec{F}_b)_{ij}$ proportional to $T_{i,j}$ (the minimum thickness of elements i and j) so the formulation of interactive forces has the desired property that it obeys Newton's 3rd Law (i.e.: $(\vec{F}_{IA})_{ij} = -(\vec{F}_{IA})_{ji}$). This is in contrast to some other DEM models in the literature (e.g. Li et al [2014]). The minimum thickness is preferred to the average thickness, since this means that the for two bonded elements a fixed distance apart, acceleration due to elastic forces is bounded, even when the thickness of one of the elements approaches zero.

The frictional damping force has components that damp both the relative radial velocity and relative transverse velocities of the two elements. If \vec{r}^\perp is the direction vector perpendicular to \vec{r} , and $P_{\vec{r}}$ and $P_{\vec{r}^\perp}$ are the projection matrices that project onto \vec{r} and \vec{r}^\perp respectively, then the frictional damping force is given by

$$(\vec{F}_d)_{ij} = \left(-c_r P_{\vec{r}} - c_t P_{\vec{r}^\perp} \right) \cdot (\vec{u}_i - \vec{u}_j) \quad (8)$$

Here c_r and c_t are the radial and transverse drag coefficients. For the simulation below, we set $c_r = 2\sqrt{\kappa_e}$ and $c_t = \frac{1}{4}c_r$ so that the radial elastic force is critically damped, and the

¹⁹⁶ transverse damping is sub critical. The damping forces are implemented using an implicit
¹⁹⁷ time stepping scheme, to avoid stability issues for very small elements (details found in
¹⁹⁸ Appendix B).

¹⁹⁹ The effectiveness of the repulsive forces can be seen in Figure 1 which shows an un-
²⁰⁰ coupled simulation where ice elements drift westward into a bay, and eventually come to
²⁰¹ rest with minimal overlap between elements. The effectiveness of the numerical bonds is
²⁰² demonstrated in Figure 2 tabular icebergs (constructed from many ice elements bonded
²⁰³ together) and individual icebergs (unbonded elements) drift together towards a convex
²⁰⁴ coast line. When the tabular icebergs arrive at the coast, they bump into the coastline
²⁰⁵ and begin to rotate, influencing the paths of the other icebergs. In this example we see
²⁰⁶ that modeling large structures using small elements bonded together, allows us to achieve
²⁰⁷ large-scale structure and rotational motion, without having to include an equation for the
²⁰⁸ angular momentum of the elements (as discussed in Jakobsen [2001]).

2.3. Element geometry and packing

²⁰⁹ Elements are packed differently depending on the shape of the elements. For all simula-
²¹⁰ tions in this study, we use elements whose surface areas are equally-sized regular hexagons.
²¹¹ In order to pack these elements together, the hexagonal elements are initially arranged in
²¹² a staggered lattice, with each element bonded to the adjacent elements (see Figure 3a).
²¹³ In this arrangement, each element (away from the edges) is bonded to six other elements.
²¹⁴ The bonds between elements form a pattern of equilateral triangles, which give the larger
²¹⁵ structure rigidity.

²¹⁶ Some experiments were also performed using rectangular elements, arranged in a reg-
²¹⁷ ular (non-staggered) lattice. In this case, each element forms four bonds with adjacent

elements. However, the resultant structures were found to be much less rigid and tended to collapse when sufficient forces was applied. For this reason, hexagonal elements were preferred.

2.4. Ocean-ice and ice-ocean coupling

The LIISM model is coupled to the ocean model via a two-way synchronous coupling, meaning that ocean model fields are passed to the LIISM model and the LIISM model fields are passed back to the ocean model at every time step. Passing fields between the two models involves interpolating fields between the Eulerian grid of the ocean model and the ‘Lagrangian grid’ of the LIISM model (i.e.: onto the ice elements).

The coupling from the ocean model to the LIISM model is straight forward: at every time step, the ocean mixed layer temperature, salinity, velocity and sea-ice concentration are passed from the ocean model to the LIISM model, to be used in the momentum and thermodynamics equations of the ice elements. Within the LIISM model, the ocean model fields are interpolated onto the Lagrangian grid using a bilinear interpolation scheme. The LIISM model is not sensitive to the chosen interpolation scheme.

The coupling in the other direction, from the LIISM model to the ocean model, is more complex. The LIISM model influences the ocean by: (i) applying a pressure to the ocean surface, (ii) applying a heat, salinity and mass flux to the ocean, associated with ice melting, and (iii) affecting the upper ocean boundary condition by applying a no slip boundary condition and frictional velocity beneath the ice. Fields from the LIISM model are interpolated from the Lagrangian grid to the Eulerian ocean grid before they are passed to the ocean model. Since the LIISM model applies large pressures to the ocean surface, the ocean model is sensitive to the interpolation scheme used to map the

²⁴⁰ LIISM fields to the ocean grid. Sudden jumps to the ocean surface pressure can trigger
²⁴¹ tsunamis within the ocean model, making the ocean model become unstable.

²⁴² The interpolation of the LIISM fields onto the ocean grid is done in a way that is
²⁴³ consistent with the shape of the elements in the LIISM model (see Section 2.3). Fields
²⁴⁴ are ‘spread’ to the ocean model by exactly calculating what fraction of an element’s
²⁴⁵ surface area lies in a particular grid box, and dividing the field in proportion to this
²⁴⁶ fraction. For example, consider an element which has a hexagonal surface area in the
²⁴⁷ LIISM model, which is positioned such that it intersects four ocean grid cells (Figure
²⁴⁸ 3b). In this situation, the mass of the element is divided between these four ocean cells
²⁴⁹ in proportion to the overlap area between the hexagonal element and the grid cell (this
²⁵⁰ fraction is shown by the colors in 3b). An advantage of this approach is that there are no
²⁵¹ jumps in pressure as an element moves from one grid cell to another.

²⁵² The numerical calculation of the intersection between hexagons and the ocean grid is
²⁵³ simplified by dividing the hexagon into 6 equilateral triangles. This method allows for the
²⁵⁴ intersection to be found even when the hexagon is not aligned with the grid. The LIISM
²⁵⁵ model can be run using hexagonal or rectangular elements.

²⁵⁶ The field-spreading scheme is coded with the restriction that an element’s area can only
²⁵⁷ intersect a maximum of four ocean grid cells at a time. A consequence of this is that this
²⁵⁸ sets a limit on the maximum size of elements that can be represented using this model,
²⁵⁹ i.e.: the longest horizontal dimension of an ice element must be smaller than the ocean
²⁶⁰ grid spacing. Larger ice structures are constructed by bonding together smaller elements.

2.5. Thermodynamics

261 The ice elements decay according to a number of melt parameterizations. As the ice
262 elements melt, their mass decreases, and the appropriate salt, mass and heat fluxes are
263 passed to the ocean. In this section we described the melt parametrization for bonded,
264 unbonded and partially bonded elements.

265 As mentioned above, ice elements which do not interact with other elements are modeled
266 identically to the point particle icebergs described in Martin and Adcroft [2010]. These
267 elements melt according to three semi-empirical parametrization for melt commonly used
268 in previous iceberg studies [Gladstone et al , 2001; Martin and Adcroft , 2010]. Three
269 types of iceberg melting are used: basal melt, M_b , melt due to wave erosion, M_e and melt
270 due to buoyant convection, M_v . M_e and M_v are applied to the sides of the ice element,
271 while M_b is applied at the ice element base. The details of M_b . M_v and M_e are given in
272 Appendix A.

273 When multiple elements are bonded together to form larger structures, it is no long
274 appropriate to use the parameterizations for melt developed for individual point-particle
275 icebergs. An element which is completely surrounded by other elements, is meant to
276 represent a piece of ice in the middle of a large structure, and hence will not experience
277 a melt at its sides due to wave erosion or buoyant convection. Also, the iceberg basal
278 melt rate, M_b described above is based on boundary layer theory of flow past a finite
279 plate, and is only appropriate for basal surfaces where the distance from the leading edge
280 is sufficiently small [Eckert , 1950; Weeks and Campbell , 1973]. For an element in the
281 interior of large structures, the distance from the edge of the structure is large, and so
282 using M_b for the basal melt is not appropriate. Instead, the basal melt, M_s is determined

²⁸³ using the three equation model for basal melt, which is a typical melting parametrization
²⁸⁴ beneath used beneath ice shelves [Holland and Jenkins , 1999].

When using both individual elements and bonded elements in the same simulation, we determine which melt rate parameterizations to use based on the amount of bonds that each element has. An element which is in the center of a large structure will form the maximum number of bonds, while unbonded elements form zero bonds. If maximum number of bonds that an element can form (given the shape of the element) is N_{max} , and the number bonds that an element has is N_b , then the side melt and bottom melt for that element are given by

$$M_{side} = \frac{(N_{max} - N_b)}{N_{max}}(M_v + M_e) \quad (9)$$

and

$$M_{bottom} = \frac{(N_{max} - N_b)}{N_{max}}M_b + \frac{N_b}{N_{max}}M_s \quad (10)$$

²⁸⁵ respectively. In this way, elements with no bonds, melt like point particle icebergs, ele-
²⁸⁶ ments at the center of large structures melt like ice shelves, and elements at the sides of
²⁸⁷ large structures have a combination of iceberg side and basal melt, and ice shelf melt.

2.6. Algorithms and computational efficiency

²⁸⁸ Including interactions between elements leads to an increase in the computational com-
²⁸⁹ plexity of the model. In this subsection we comment on some of the algorithmic proce-
²⁹⁰ dures that have been used to increase the computational efficiency. Readers who are not
²⁹¹ interested in this more technical side of the model should skip this section.

2.6.1. Time stepping

293 The ice elements in the LIISM model are advected using a semi-implicit velocity Verlet
294 time-stepping scheme. The velocity verlet time stepping scheme is commonly used in DEM
295 models in video games because it is computational efficient and has desirable stability
296 properties [Jakobsen , 2001]. This time stepping scheme was preferred to the Runge-
297 Kutta 4, which was used in the iceberg model of Martin and Adcroft [2010] since, the
298 Verlet time stepping only requires one calculation of the interactive forces per time step
299 (while the Runge-Kutta scheme requires the interactive forces to be calculated four times).
300 Since the calculation of the interactive forces is one of the most computationally expensive
301 part of the algorithm, the Verlet scheme leads to a significant increase in the speed of the
302 model. We note that the Verlet scheme used in the LIISM contains a small modification
303 of the original (fully explicit) velocity Verlet time stepping scheme in that damping terms
304 are treated implicitly (which increases the numerical stability). The details of this time
305 stepping scheme are outlined in Appendix B.

306 2.6.2. Interactions and Bonds

307 At every time step, we calculate the force on each element due to interactions with every
308 other element. In principle, this involves order n^2 operations (for n elements). However,
309 since each element only has repulsive interactions with elements that are less than one
310 ocean grid cell away, and each element only has bonded interactions with a small number
311 of other elements, we are able to reduce the complexity of the system.

312 The complexity reduction is achieved by storing the element data in an efficient way
313 that prevents having to search through all element pairs to check if they are close to
314 one another or are bonded with one another. The data storage system works as follows:
315 pointers to the memory structures containing each element are stored in linked list data

316 structures, which allow elements to be added and removed from the lists easily without
317 restructuring the entire list. Instead of using one list for all the elements on a processor,
318 we use a separate linked list for each ocean grid cell. When an element moves between
319 ocean grid cells, it is removed from its original list and added to the list corresponding to
320 its new ocean grid cell. Since the area of elements has to be smaller than the area of an
321 ocean grid cell, the critical interaction critical interaction length scale (equation 5) is less
322 than the length of a grid cell. This means that elements only experience repulsive forces
323 with elements in the same ocean grid cell, or in one of the 8 adjacent cells. Limiting the
324 possible repulsive interactions to elements in the 9 linked lists substantially reduces the
325 computational time needed to calculate the total interactive force.

326 Bonded interactions are handled slightly differently. Each bond is assigned a piece of
327 memory. Each ice element contains a linked list of each of its bonds (typically up to six
328 bonds per element). At each time step, the code traverses the lists of bonded elements,
329 and adds a bonded force corresponding to these bond. The bonded force is only applied
330 if $\vec{r}_{i,j} > L_{ij}$, to avoid double counting an interaction. Having a list of bonds stored with
331 each element reduces the computational complexity of bonded interactions from order n^2
332 to order n. Handling bonded attractive forces separately to the repulsive and non-bonded
333 forces means that we do not need to check whether two elements are bonded, which further
334 increases the computational efficiency.

335 **2.6.3. Parallelization and halos**

336 The LIISM model runs on multiple processors in parallel. When elements move from
337 an ocean cell on one processor to an ocean cell on a second processor, the memory has to
338 be passed from one processor the next, added and removed to the appropriate lists and

339 the memory has to be allocated and deallocated correctly. Element interactions across
340 the edge of processors are handled using computational halos. A computational halo is a
341 copy of the edge of a one processor which is appended to the edge of a second processor,
342 so that the first processor can ‘see’ the second processor during a time step. Before a
343 time step, elements at the edges of each processor are copied onto the halos of adjacent
344 processors so that they can be used in calculating the interactive forces. After each time
345 step, these halos are removed, and the process is repeated. These halo updates are one
346 of the most computationally expensive parts of the LIISM model.

347 Keeping track of pairs of bonded elements that move across a processor edge requires
348 a lot of book keeping since bonds have to be severed and reconnected. Details of how
349 the bonds are broken and reconnected across processor boundaries are provided in Ap-
350 pendix C.

3. Experiment Setup

351 The introduction of Lagrangian elements, numerical bonds and interpolation schemes
352 between the Eulerian and Lagrangian grids (discussed in Section 2) means that we are
353 now able to model ice shelf cavities which undergo large calving events. We demonstrate
354 this capability by performing numerical experiments with the LIISM model coupled to
355 the MOM6 ocean model [reference].

3.1. MISOMIP configuration

356 In order for our (pre-calving) simulations to be easily comparable to previous models
357 of ice shelf cavities, we use an experimental setup based on the configuration created for
358 the Marine Ice Ocean Modeling Inter-comparison Project (MISOMIP) [Asay-Davis et al

, 2016]. The MISOMIP configuration was developed as a standardize configuration to allow for the comparison between various ocean-ice coupled models. The configuration consists of an idealized ice shelf in a rectangular domain. The domain is $L_x = 80\text{km}$ wide and $L_y = 480\text{km}$ long, and contains an ice shelf which is grounded on the south side of the domain and has an ice front at $y=650\text{km}$. The ice thickness and bottom topography of this setup are shown in Figure 4a and 4b respectively, with the grounding line position drawn in for reference. The configuration is the same as that of the Ocean0 setup in the MISOMIP, with three changes made:

1. The ‘calving criteria’ used in the MISOMIP study (which states that all points in the ice shelf with thickness less than 100m are set to zero thickness) has not been used.
2. The ice shelf has been thickened on the flanks of the domain, so that the latitude of the grounding line increases away from the center of the ice shelf.
3. The ice shelf is configured to be symmetric about its center line. This was achieved by using the average of the left and right flank of the ice shelf thickness.

These three changes were made in order to make the circulation beneath the ice shelf easier to interpret.

The LIISM model is coupled to the MOM6 ocean model. The ocean model is run in using vertical coordinate system which is a hybrid between a sigma level and a z-level coordinate. In particular, model layers bend underneath the ice shelf as they would in a sigma model, but collapse to zero thickness when they intersect with bottom topography, as they would in a z-level model. The coordinate system was achieve using ALE regridding-remapping scheme. The model used a horizontal resolution of 2km, and 36 vertical layers. All simulation were repeated using the ocean model is run layered mode (select results are

382 shown in the supplementary material). Ocean parameters are as specified in the MISOMIP
383 configuration [Asay-Davis et al , 2016], and are shown in Table 1. The simulation is
384 initially at rest, with horizontally uniform initial ocean temperature (Figure 5a) and
385 salinity profiles that vary linearly between specified surface and bottom values. The
386 initial surface temperature and salinity are $T_t = -1.9^{\circ}\text{C}$ and $S_t = 33.8 \text{ psu}$, respectively.
387 The initial temperature and salinity at the depth H_{ocean} are $T_b = 1.0^{\circ}\text{C}$ and $S_b = 34.7$
388 psu. The maximum ocean depth is $H_{ocean} = 720 \text{ m}$. A sponge layer is used on the
389 northern boundary of which relaxes back to the initial temperature and salinity with a
390 relaxation time scale of $\tau = 0.1 \text{ days}$. Melting is set to zero for cells where the ocean
391 column thickness is less than 10m to avoid using more energy to melt ice than is present
392 in the water column.

3.2. Initializing Lagrangian elements:

393 Ice elements in the LIISM model are set to be hexagonal and are arranged in a regular
394 staggered lattice (as discussed in Section 2.3). The apothem of the gridded hexagons are
395 initially set to $A = 0.85 \text{ km}$. Recall that the element size must be smaller than the ocean
396 grid spacing (i.e.: $2A < \Delta x$). Gaps along the boundary are filled in with using smaller
397 elements so that the total ice shelf area is preserved. The initial mass of the ice elements is
398 determined by a preprocessing inversion step, which is the inverse of the 'mass-spreading'
399 interpolation procedure discussed in Section 2.3.

400 Figure 4c shows what the ice shelf draft would be if the draft were calculated from
401 the mass of elements in each ocean grid cell without spreading an elements mass across
402 neighboring cells (i.e.: treating elements as point masses). Figure 4b shows the draft after
403 spreading the mass across grid cells. When the mass spreading interpolation scheme is

not used, grid artifacts seen in the ice shelf draft (Figure 4c). The grid artifacts are much reduced when the mass spreading interpolation is used (Figure 4b).

3.3. Numerical experiment

1. Static ice shelf experiment:

In the first experiment, we use a static ice shelf where the velocity of all ice elements is set to zero. In this experiment, the ice shelf is thermodynamically active and is able to ‘melt’ but has a constant thickness (as was done in the Ocean0 setup in the MISOMIP [Asay-Davis et al , 2016]). In this setup, ice shelf melting generates a temperature and salinity flux into the ocean, but does not change the thickness of the ice shelf. This can be thought to represent an ice shelf in dynamic equilibrium where the melt is exactly balanced ice shelf advection.

Results of the static ice shelf experiment using the LISSM model are compared to the results from an existing Eulerian ice shelf cavity model [Goldberg et al , 2012], run in an identical configuration (using the ice draft from Figure 4b). The simulations in the Lagrangian and Eulerian are compared after 5 years of models time.

2. Tabular iceberg calving:

Next, we preform a numerical experiment which demonstrates capabilities of the LIISM model that can not be performed by traditional Eulerian ice shelf models. In this experiments we break off a large piece of the the ice shelf and allow it to drift into the ocean as a tabular iceberg.

All ice elements initially within a 14.4 km radius of the center of the ice front are allowed to move freely while the other ice elements continue to be held are stationary. Ice elements less than 12 km from the center of the ice front, are bonded together to form a semi-

426 circular tabular iceberg. A ring of elements whose distance from the ice front center is
427 ≥ 12 km, but ≤ 14.4 km are allowed to move freely, but have all their bonds removed.
428 Elements in this half annulus represent fragments of the ice shelf with calve into small
429 pieces during a large calving event, and also allow the giant icebergs to move away from
430 the ice shelf cavity more easily.

431 A wind stress $\vec{\tau} = <0.05, 0.05> \frac{N}{m^2}$ is applied to drive the tabular iceberg away from the
432 ice shelf cavity. Perturbation experiments were run using other wind stress values. In this
433 experiment, the ice is allowed to decay as it melts. The tabular iceberg calving experiment
434 is initialized using the ocean state from the end of the static ice shelf experiment (after 5
435 years).

4. Results

4.1. Static ice shelf experiment

436 The LIISM results from the static ice shelf experiment fit well within the current under-
437 standing of ice-shelf cavity circulations base on ice shelf observations [MacAyeal , 1984;
438 Lewis and Perkin , 1986; Jacobs et al , 2011] and previous modeling efforts [Determan and
439 Gerdes , 1994; Holland and Feltham , 2006; Losch , 2008]. The initial water temperatures
440 inside the domain are warmer than the in-situ freezing point, and cause melting at the
441 ice-shelf base. The melt water entering the domain is more buoyant than the water around
442 it, and rises along the ice shelf as a cool fresh plume (Figure 5b, c). As the plume rises, it
443 entrains ambient water causing a warming of the upper ocean (Figure 5b). This injection
444 of buoyancy at depth drives a clockwise circulation outside of the ice shelf cavity (Figure
445 7a), providing the ice shelf cavity with a continuous supply of warm water which provides
446 the thermal energy required for continuous ice shelf melt.

447 The highest melt rates are seen within 100km of the grounding line (Figure 6a). These
448 elevated melt rates are caused by the presence of warm water (Figure 6d) and increased
449 ocean velocities (Figure 6c) near the grounding line. Elevated melt rates are also seen
450 near the ice front, caused by strong currents running along the ice shelf front.

451 **Comparison of LIISM and Eulerian ice shelf models**

452 The LIISM results from the static ice shelf experiment are qualitatively similar to most
453 of the simulations from the MISOMIP experiment [Asay-Davis et al , 2016], which use a
454 similar configuration. To get a quantitative comparison, we compare the LIISM results
455 to a simulation using an Eulerian ice shelf model using an identical configuration. The
456 results show that two simulations have similar circulations (Figures 7), melt rates and
457 temperature/salinity profiles (see supplementary materials). The differences between the
458 barotropic stream function of the two simulations (for example) are two orders of mag-
459 nitude smaller than the differences between two simulations using the same Eulerian ice
460 shelf with difference vertical coordinate systems [double check that this is correct].

461 The good agreement between the Eulerian and Lagrangian simulations is not too sur-
462 prising since the two models are coupled to the same ocean model. Recall that the role
463 of the ice shelf model in these simulations is to (i) apply a pressure to the ocean surface,
464 (ii) provide melt fluxes based on the three equation model, and (iii) alter the upper ocean
465 boundary condition below the ice shelf. The agreement between the Eulerian
466 and Lagrangian simulations is a confirmation that these three tasks are being done cor-
467 rectly within the LIISM model, and that the LIISM is able to model sub ice shelf
468 cavities as well as the Eulerian model does. This is a good starting point for moving
469 beyond the capabilities of the Eulerian model.

4.2. Tabular iceberg calving

470 The tabular iceberg calving experiment demonstrates that the model is able to simulate
471 a tabular iceberg being calved from an ice shelf. After the iceberg calves (referred to at
472 time t=0 days), the iceberg drifts to the northward east, driven by the wind and steered
473 by the Coriolis force (Figure 8, 9). After the iceberg has calved away from the ice shelf,
474 we observed a warming of the surface waters near the near the ice front and iceberg edge
475 (Figure 10). This surface warming is caused by an upwelling of the warmer waters from
476 beneath the ice shelf and iceberg. As the icebergs drifts away from the ice front, these
477 warmer waters remain in the wake of the iceberg. The signature of upwelling water in
478 the wake of a drifting tabular iceberg bears some similarity to satellite observations of
479 streaks of increased ocean color near to tabular iceberg in the Southern Ocean [Duprat
480 et al , 2016], suggesting that the increased productivity around iceberg may be driven by
481 upwelling water delivering nutrients to the surface.

482 The motion of the iceberg disturbs the ocean surface which drives ocean velocities
483 through out the water column 11. The elevated velocities around the tabular iceberg lead
484 to increased vertical mixing in the vicinity of the iceberg, which alters the stratification
485 of the water column (Figure 9).

486 The increased ocean velocities and increased surface temperatures cause elevated melt
487 rates at the base of the ice shelf and iceberg S8. Large melt rates are observed at the
488 new ice shelf front and on the rounded side of the iceberg (Figure S8a), where the iceberg
489 calving calving has created an ice cliff at the edge of the ice shelf and iceberg. These
490 sharp ice fronts allows for large ocean currents (Figure S8c), which drive the elevated
491 melt rates. This will smooth out the ice front over time, and make it less sharp. While

492 this is likely a real phenomena that could be observed in the real world, we should be
493 wary of the modeled velocities at ice cliffs, since large changes in ice shelf thicknesses are
494 often associated with numerical pressure gradient errors which can drive spurious motion.

495 As mentioned above, the direction (and speed) of the iceberg drift is largely determined
496 by the wind speed and direction. Perturbation experiments using different wind stresses
497 showed that the iceberg drifted to the north east for positive zonal and to the north west
498 for negative zonal velocities. For wind stresses less than $\tau = ???$ the iceberg did not move
499 away from the ice shelf. While this result is partly an artifact of the artificial shape of the
500 calving iceberg, it is also consistent with Bassis and Jacobs [2013] who noted that calving
501 is a two step process consisting of (i) ice shelf breaking and (ii) iceberg detachment. The
502 results here suggest that strong wind may be required to drive large tabular icebergs away
503 from their mother glaciers.

504 Finally, we note that the numerical bond in the LIISM model are in fact needed in
505 order to allow the tabular iceberg to retain its shape. Comparing the iceberg calving
506 simulation with an identical simulation with all numerical bonds removed shows that in
507 the absence of the bonds, the ice elements quickly disperse (Figure 13). In this case, the
508 model behavior is more similar to an ice shelf disintegration and does not create a cohesive
509 tabular iceberg.

5. Discussion

510 In order to accurately project future sea level, it is likely that we will need to develop
511 fully-coupled global general climate models (GCM's) with dynamic ice-shelf cavities which
512 are able to melt, break and interact with the ocean in physically realistic ways. In the
513 sections above, we have seen that constructing ice shelves out of Lagrangian elements is a

514 potentially useful method for introducing breakable ice shelves and tabular icebergs into
515 climate models. In this section we briefly discuss a few of the things which still need to
516 be done in order to introduce this technology into next generation GCM's.

517 One element which is missing from the LIISM ice shelf is that the ice shelf is not
518 dynamic. Real-world ice shelves are non-Newtonian fluids which are able to flow, allowing
519 the ice shelf geometry to change over time. Much progress has been made in modeling
520 ice-shelf flows in an Eulerian framework [Grosfeld and Sandhger , 2004; Goldberg et al
521 , 2012; De Rydt and Gudmundsson , 2016]. A challenge will be to develop similar ice
522 dynamics models in a Lagrangian framework. This can perhaps be achieved using smooth
523 particle hydrodynamics (SPH) methods, which allow partial differential equations to be
524 solved on a Lagrangian grid [Liu and Liu , 2010; Pan et al , 2013]. However, it is presently
525 unclear how one would evolve the numerical bonds over time, so the bonds could still be
526 used to hold the ice shelf and tabular icebergs together. This may involve performing a
527 regridding of the ice element or a regridding of the numerical bonds after several ice time
528 steps, or perhaps allowing the numerical bonds to break and form in a dynamic way.

529 The other major innovation which will need to be introduced is a method for breaking
530 numerical bonds. This is essentially equivalent to determining a ice shelf calving law, and
531 is a famously difficult problem. One possible way that this could be done is to break
532 bonds when the elastic stress in the bond is larger than a given yield stress of that bond.

533 The yield stress in the bond would likely be proportional to the ice thickness. The bond
534 strength could also evolve dynamically as bonds get 'damaged'. The evolution of bond
535 damage could be tracked using damage mechanics, as has been done in some Eulerian ice
536 shelf studies [Pralong and Funk , 2005; Borstad et al , 2012].

537 In addition to these two problems, more work needs to be done to determine the in-
538 teraction between tabular icebergs and sea ice, as the presence of sea ice can arrest the
539 motion of tabular icebergs and the presence of icebergs likely affects sea ice formation
540 and dynamics. A possible path towards this is to model sea ice using a Lagrangian grid
541 [Hopkins , 1996; Li et al , 2014], and to treat sea ice - iceberg interactions in the same
542 way that iceberg - iceberg interactions are treated in this study. A number of preliminary
543 experiments have been run using the LIISM model with some ice element representing col-
544 lections of sea ice flows, and have yielded interesting results (to be presented elsewhere).
545 Finally, there are a number of open questions about how to correctly link tabular ice-
546 bergs to ocean biology by allowing for icebergs to have nutrient concentration (especially
547 iron). These will need to be considered in order to model the primary productivity around
548 tabular icebergs.

549 Finally, there are a number of open questions associated with introducing giant tabular
550 icebergs into climate models: (i) how to correctly link tabular icebergs' melt water fluxes
551 to ocean biology, (ii) how to deal with giant calving events in small ensemble simulations
552 where one calving even can skew the ensemble statistics, (iii) how to introduce tabular
553 icebergs into models which do not use a fully dynamic ice sheet, and (iv) how to model
554 iceberg breakup and fracturing. These and other questions will need to be answered in
555 order to achieve physically realistic climate models with tabular icebergs and breaking ice
556 shelves.

6. Appendix A

6.1. Environmental forces on ice elements

The non-interactive forces on an ice element are as described in [Martin and Adcroft , 2010], and are repeated here for completeness. The force on an element due to air (a), ocean (o) and sea ice (si) drag are given by

$$(\vec{F}_a) = \rho_a(0.5c_{a,v}WF + c_{a,h}LW)|\vec{u}_a - \vec{u}|(\vec{u}_a - \vec{u}), \quad (11)$$

$$(\vec{F}_o) = \rho_o(0.5c_{o,v}W(D - T_{si})F + c_{o,h}LW)|\vec{u}_o - \vec{u}|(\vec{u}_o - \vec{u}), \quad (12)$$

$$(\vec{F}_{si}) = \rho_{si}(0.5c_{si,v}WT_{si}F + c_{si,h}LW)|\vec{u}_{si} - \vec{u}|(\vec{u}_{si} - \vec{u}). \quad (13)$$

557 Here ρ_a , ρ_o , ρ_{si} , are the density of air, ocean and sea ice, respectively. $c_{a,v}$, $c_{o,v}$ and $c_{si,v}$
 558 are the vertical drag coefficients with air, ocean and sea ice, while $c_{a,h}$, $c_{o,h}$ and $c_{si,h}$ are
 559 the respective horizontal drag coefficients. Here \vec{u}_a , \vec{u}_o , \vec{u}_{si} , are the velocities air, ocean
 560 and sea ice, respectively. L, W, T, F and D are the length, width, thickness, freeboard
 561 and draft of the ice element. The element thickness is related to the draft and freeboard
 562 by $T = F + D$ and $D = \frac{\rho}{\rho_o}T$, where ρ is the ice element density.

The wave radiation force (\vec{F}_R) is given by

$$\vec{F}_R = \frac{1}{2}\rho_o c_r g a \min(a, F) 2 \frac{WL}{W + L} \frac{\vec{v}_a}{|\vec{v}_a|} \quad (14)$$

where g is the acceleration due to gravity, a is the wave amplitude empirically related to the wind speed by $a = 0.010125|\vec{v}_a - \vec{v}_o|$, and c_{wd} is the wave drag coefficient defined as

$$c_{wd} = 0.06 \min \left(\max \left[0, \frac{L - L_c}{L_t - L_c} \right], 1 \right), \quad (15)$$

563 where $L_w = 0.32|\vec{v}_a - \vec{v}_o|^2$ is an empirical wave length, $L_c = 0.125L_w$ is the cutoff length,
 564 and $L_t = 0.25L_w$ is the upper limit.

The pressure gradient force is approximated as a force due to sea surface slope and given by

$$\vec{F}_{SS} = -Mg\vec{\nabla}\eta \quad (16)$$

where η is the sea surface height.

6.2. Melt rate parametrization

As discussed in Section 2.5, unbounded ice elements in the LIISM model decay according to parameterizations for iceberg decay typically used in iceberg drift models [Martin and Adcroft , 2010], while ice elements within larger ice structures have only a basal melt given by the three equation model [Holland and Jenkins , 1999] .

For unbonded ice elements, the element thickness decays at due to basal melt at a rate M_b , while the length and width of the elements decay as a result of melt due to wave erosion, M_e and melt due to buoyant convection, M_v . Following Martin and Adcroft [2010], the basal melt rate, wave erosion melt rate, and buoyant convection melt rate are parameterized by

$$M_b = 0.58|\vec{v} - \vec{v}_0|^{0.8} \frac{\tilde{T}_0 - \tilde{T}}{L^{0.2}} \quad (17)$$

$$M_e = \frac{1}{12}S_s \left(1 + \cos [\pi A_i^3] \right) \left(\tilde{T}_0 + 2 \right), \quad (18)$$

$$M_v = \left(7.62 \times 10^{-3} \right) \tilde{T}_0 + \left(1.29 \times 10^{-3} \right) \tilde{T}_0^2. \quad (19)$$

\tilde{T} is the effective iceberg temperature and is set to $\tilde{T} = 4^\circ\text{C}$, \tilde{T}_0 is the temperature at the top of the ocean, A_i is the sea ice area fraction, and S_s is the sea state, which is given by the Beaufort scale

$$S_s = \frac{2}{3}|\vec{u}_a - \vec{u}_o|^{\frac{1}{2}} + \frac{1}{10}|\vec{u}_a - \vec{u}_o| \quad (20)$$

All three melt rates are in units of meters per day.

571 For elements inside larger structures, the melt due to wave erosion and melt due to
 572 buoyant convection are set to zero, and the basal melt, M_s is given by the standard three
 573 equation model [Holland and Jenkins , 1999].

7. Appendix B

7.1. Modified Verlet Algorithm

574 The LIISM model uses a version velocity verlet algorithm, which has been modified
 575 to allow part of the forcing to be calculated implicitly. The traditional velocity verlet
 576 algorithm is commonly used in molecular dynamics, as it is simple to implement, second
 577 order accurate and computationally efficient [Swope et al , 1982; Omelyan et al , 2002].
 578 Here we modify the tradition scheme to allow for the drag forces to be modeled implicitly,
 579 which prevents large accelerations for element's whose mass approaches zero. To do
 580 this, we modify the traditional verlet algorithm to include both an implicit and explicit
 581 acceleration, $a(t) = a_{exp}(t) + a_{imp}(t)$. The explicit acceleration, $a_{exp}(t)$ includes all forcing
 582 terms which depend only on the previous time step, while the implicit acceleration, $a_{imp}(t)$
 583 includes forcing terms which depend on the current time step (in particular the drag and
 584 Coriolis forces).

585 Using a time step of Δt and the notation $t_{n+1} = t_n + (\Delta t)$, the modified velocity verlet
 586 scheme can be written as:

587 1) $x(t_{n+1}) = x(t_n) + u(t_n)\Delta t + \frac{1}{2}\Delta t^2 \left(a_{exp}(t_n) + a_{imp}(t_n) \right)$.

588 2) Calculate $a_{exp}(t_{n+1})$ and $a_{imp}(t_{n+1})$

589 3) $u(t_{n+1}) = u(t_n) + \frac{\Delta t}{2} \left(a_{exp}(t_n) + a_{exp}(t_{n+1}) \right) + (\Delta t)a_{imp}(t_{n+1})$

590 This scheme reduces to the traditional velocity verlet when a_{imp} is set to zero. Note that
 591 at step 2, $a_{exp}(t_{n+1})$ is an explicit function of $x(t_{n+1})$ and other qualities evaluated at time

⁵⁹² t_n , while $a_{imp}(t_{n+1})$ additionally depends on $u(t_{n+1})$ (and needs to be solved implicitly).

⁵⁹³ For this reason, steps 2 and 3 need to be solved simultaneously, as described in the next

⁵⁹⁴ section.

⁵⁹⁵ In equation (1), the forces due to ocean drag, atmospheric drag and sea ice drag are
⁵⁹⁶ treated implicitly. The force due to sea surface slope and wave radiation are treated
⁵⁹⁷ explicitly. The Coriolis term is handled using Crank-Nicolson scheme so that half of the
⁵⁹⁸ effect is implicit and half is explicit. The elastic part of the interactive forces is treated
⁵⁹⁹ explicitly, while the interactive damping is handled semi-implicitly in that the drag force
⁶⁰⁰ on element A by element B depends on the velocity of elements A and B evaluated at
⁶⁰¹ time t_{n+1} and t_n , respectively.

7.2. Solving for the velocity implicitly

Since this modified scheme contains some forcing terms which are handled implicitly, steps 2 and 3 need to be solved together. We demonstrate how this is done, using a simplified one-dimensional version of equation (1), neglecting the atmospheric drag, sea ice drag and Coriolis force, so that the only implicitly treated term is the ocean drag. We also define an explicit force F_{exp} , which accounts for all forces not proportional the element velocity. With these simplifications, the implicit and explicit accelerations are

$$a_{exp} = \frac{1}{M}(\vec{F}_{exp}) \quad (21)$$

$$a_{imp} = \frac{1}{M}(F_W) \quad (22)$$

The ocean drag force at time t_{n+1} is modeled (mostly) implicitly as

$$F_W(t_{n+1}) = c_w |u_w(t_n) - u(t_n)|(u_w(t_n) - u(t_{n+1})) \quad (23)$$

Step 3 of the modified velocity verlet scheme can be rewritten by introducing an intermediate velocity u^* , which only depends on the velocity and acceleration at time t_n ,

$$u^*(t_n) = u(t_n) + \frac{1}{2}(\Delta t)a(t_n). \quad (24)$$

Using this, the updated velocity (Step 3) can be written

$$u(t_{n+1}) = u^*(t_n) + \frac{\Delta t}{2}a_{exp}(t_{n+1}) + (\Delta t)a_{imp}(t_{n+1}). \quad (25)$$

Including the forcing terms into this equations gives

$$u(t_{n+1}) = u^*(t_n) + \frac{\Delta t}{2M}(F_{exp}(t_{n+1})) + \frac{\Delta t}{M} \left(c_w |u_w(t_n) - u(t_n)| (u_w(t_n) - u(t_{n+1})) \right) \quad (26)$$

Solving for $u(t_{n+1})$ in terms of quantities which only depend on the previous time step gives

$$u(t_{n+1}) = \frac{u^*(t_n) + \frac{\Delta t}{2M}(F_{exp}(t_{n+1})) + \frac{\Delta t}{M} \left(c_w |u_w(t_n) - u(t_n)| (u_w(t_n)) \right)}{\left(1 + \frac{\Delta t}{M} c_w |u_w(t_n) - u(t_n)| \right)} \quad (27)$$

Once the $u(t_{n+1})$ has been found, it can be used to calculated the explicit and implicit accelerations, which are required for the next time step.

Finally, we note that the the drag term (equation 23) is not entirely implicit, since the element velocity inside the absolute value is evaluated at time t_n , rather than at time t_{n+1} . This is done so that we can solve for the updated velocity exactly. One consequence of this is that it gives rise to a small oscillation in the element velocity. This oscillation is addressed by using a predictive corrective scheme: once you have solved for a first guess of the velocity at time t_{n+1} , this estimate of the velocity is used to update the estimate of the drag force (i.e.: inside the absolute value signs). Using the updated drag, you can now repeat the process described above to find an improved estimate of the velocity. We found that two iterations were sufficient to remove the unwanted oscillation.

613 The procedure described in this section is easily extended to include more forcing terms
 614 and two dimensions (where it involves inverting a 2×2 matrix).

8. Appendix C

615 Connecting bonds across processor boundaries

616 When a bonded element moves off the edge of a processor, the bond needs to be bro-
 617 ken. When the element is copied into the halo of the processor, the bond needs to be
 618 reconnected.., and then reconnected when the element is copied back

619 The basics of the bond bookkeeping work as follows. Consider an element A and an
 620 element B that are bonded together. As mentioned above, each element has a copy of
 621 the bond which is stored with the element. Let A-B be the bond stored by element A,
 622 and B-A be the bond stored by element B. Bond A-B contains a pointer which points to
 623 element B and bond B-A contains a pointer which points to element A.

624 Consider a situation where element A and B are originally on Processor 1, and then
 625 element B moves to Processor 2. When this occurs, the memory assigned to element B
 626 on processor 1 is removed, and is allocated on Processor 2. This means that the pointer
 627 to element B in bond A-B (stored in element A on Processor 1) is no longer assigned.

628 Similarly, the pointer to element A in bond B-A (stored in element B on Processor 2) is
 629 no longer assigned. Before the next time step, a halo update occurs, so that there is
 630 a copy of element A in the halo of Processor 2 and a copy of element B in the halo of
 631 Processor 1. After the halo update, the bonds A-B and B-A have to be reconnected on
 632 both Processor 1 and 2. To aid in reconnecting the bonds, a copy of the grid cell number
 633 of element B is stored in the bond A-B and a copy of the grid cell number of element A
 634 is stored in the bond B-A. We refer to this as the ‘most recent address’. Before a bond

635 is moved from one processor to another, the ‘most recent address’ is updated, so that the
636 bond can be reconnected later. To reconnect bond A-B on Processor 1 (for example), we
637 find the most recent address of element B, and search through the list of elements in the
638 grid cell corresponding to the most recent address of element B until element B is found.
639 The pointer to element B in bond A-B is reassigned and the bond is said to be connected.

640 Once all bonds are reconnected, a bond quality control is done where we loop through
641 all bonds and check that they are working properly. To check that a bond is working
642 properly is a four step process. For example, consider the bond A-B stored in element A
643 on Processor 1. To check the quality of this bond A-B, we use the following four steps:

- 644 1. Check that the pointer to element B is assigned on bond A-B (stored on element
645 A).
- 646 2. Check that the corresponding bond B-A exists on element B.
- 647 3. Check that a pointer to element A exists in this bond B-A.
- 648 4. Check that the element A which is being pointed to is the same element A where
649 you started.

650 All four of these tests must pass in order to make sure that the memory is correctly
651 assigned. A useful tool in this process is that each element is assigned a unique number
652 so that elements are easily identified.

9. Possibly add

9.1. Lagrangian sea ice mode

653 The addition of interactive forces between elements, means that the LIISM model can
654 be used as a Lagrangian sea ice model, following [Li et al, 2014]. In this formulation, each
655 element represents a collection of sea ice flows.

9.2. Orientation

656 We can get the orientation of iceberg by considering the bonds that they form.

657 9.2.1. DEM vs SPH

658 Note that there is some ambiguity in the literature about the definition of a Discrete
659 Element Model. In one view, to qualify as a Discrete Element Model since we do not
660 evolve the angular momentum of the elements. Since elements are allows to overlap
661 briefly, this method could be considered an example of a Smooth Particle Hydrodynamics
662 model. This same repulsive force is similar to that used by [Li et al] in the context of sea
663 ice interactions.

References

- 664 Asay-Davis, X. S., S. L. Cornford, B. K. Galton-Fenzi, R. M. Gladstone, G. H. Gudmundson, D. M. Holland, P. R. Holland, and D. F. Martin (2016), Experimental design for
665 three interrelated marine ice sheet and ocean model intercomparison projects: MIS-
666 MIP v. 3 (MISMIP+), ISOMIP v. 2 (ISOMIP+) and MISOMIP v. 1 (MISOMIP1).
667 *Geoscientific Model Development* 9, no. 7: 2471.
- 668 Arrigo, K. R., G. L. van Dijken, D. G. Ainley, M. A. Fahnestock, and T. Markus (2002).
669 Ecological impact of a large Antarctic iceberg. *Geophys. Res. Lett.*, 29(7).
- 670 Alley, R. B., H. J. Horgan, I. Joughin, K. M. Cuffey, T. K. Dupont, B. R. Parizek, S.
671 Anandakrishnan, and J. Bassis (2008), A simple law for ice-shelf calving. *Science* 322,
672 no. 5906, 1344-1344.
- 673 Bassis, J. N., and S. Jacobs (2013), Diverse calving patterns linked to glacier geometry.
674 *Nature Geoscience*, 6(10), 833-836.
- 675 Benn, D. I., C. R. Warren, and R. H. Mottram (2007). Calving processes and the dynamics
676 of calving glaciers. *Earth-Science Reviews*, 82(3), 143-179.
- 677 Bigg, G. R., Wadley, M. R., Stevens, D. P., and Johnson, J. A. (1997), Modelling the
678 dynamics and thermodynamics of icebergs. *Cold Regions Science and Technology*, 26(2),
679 113-135.
- 680 Borstad, C. P., A. Khazendar, E. Larour, M. Morlighem, E. Rignot, M. P. Schodlok, and
681 H. Seroussi (2012), A damage mechanics assessment of the Larsen B ice shelf prior to
682 collapse: Toward a physically-based calving law, *Geophys. Res. Lett.*, 39, L18502
- 683 Biddle, L. C., J. Kaiser, K. J. Heywood, A. F. Thompson and A. Jenkins (2015), Ocean
684 glider observations of iceberg-enhanced biological productivity in the northwestern Wed-
- 685

- 686 dell Sea, *Geophys. Res. Lett.*, 42, 459465.
- 687 De Rydt, J., and G. H. Gudmundsson (2016), Coupled ice shelf?ocean modeling and
688 complex grounding line retreat from a seabed ridge. *J. of Geophys. Res.: Earth Surface*,
689 121(5), 865-880.
- 690 Dunne, J.P., J.G. John,, A.J. Adcroft, S.M. Griffies, R.W. Hallberg, E. Shevliakova,
691 R.J. Stouffer, W. Cooke, K.A. Dunne, M.J Harrison, and J.P. Krasting (2012), GFDL's
692 ESM2 global coupled climate-carbon Earth System Models. Part I: Physical formulation
693 and baseline simulation characteristics. *J. of Climate*, 25(19), 6646-6665.
- 694 Depoorter, M. A., J. L. Bamber, J. A. Griggs, J. T. M. Lenaerts, Stefan RM Ligtenberg,
695 M. R. van den Broek, and G. Moholdt (2013), Calving fluxes and basal melt rates of
696 Antarctic ice shelves. *Nature*, 502(7469), 89-92.
- 697 Determan J., Gerdes R. (1994), Melting and freezing beneath ice shelves: implications
698 from a three-dimensional ocean-circulation model. *Ann. Glaciol.*, 20, 413-419.
- 699 Dowdeswell, J. A., and J. L. Bamber (2007), Keel depths of modern Antarctic icebergs
700 and implications for sea-floor scouring in the geological record. *Marine Geology*, 243(1),
701 120-131.
- 702 Duprat, L. P., G. R. Bigg, and D. J. Wilton (2016), Enhanced Southern Ocean marine
703 productivity due to fertilization by giant icebergs. *Nature Geoscience*.
- 704 Eckert, E. R. G. (1950). Introduction to the Transfer of Heat and Mass. McGraw-Hill.
- 705 Gladstone, R. M., G. R. Bigg, and K. W. Nicholls. (2001), Iceberg trajectory modeling
706 and meltwater injection in the Southern Ocean (19782012). *J. of Geophys. Res.: Oceans*,
707 106(C9), 19903-19915.

- 708 Goldberg, D. N., C. M. Little, O. V. Sergienko, A. Gnanadesikan, R. Hallberg, and M.
709 Oppenheimer (2012), Investigation of land ice?ocean interaction with a fully coupled
710 ice?ocean model: 1. Model description and behavior. *J. of Geophys. Res.: Earth Surface*,
711 117(F2).
- 712 Gladish, C. V., D. M. Holland, P. R. Holland, and S. F. Price (2012), Ice-shelf basal
713 channels in a coupled ice/ocean model. *J. of Glaciol.*, 58(212), 1227-1244.
- 714 Grosfeld K., R. Gerdes, J. Determan (1997), Thermohaline circulation and interaction
715 between ice shelf cavities and the adjacent open ocean. *J. Phys. Oceanogr.*, **102**, C7,
716 15959-15610.
- 717 Grosfeld, K., and H. Sandhger, (2004). The evolution of a coupled ice shelfocean system
718 under different climate states. *Global and Planetary Change*, 42(1), 107-132.
- 719 Holland D. M., Jenkins A. (2001), Adaptation of an isopycnic coordinate ocean model for
720 the study of circulation beneath ice shelves. *Mon. Wea. Rev.*, 129, 1905-1927.
- 721 Holland P. R. and D. L. Feltham (2006), The effects of rotation and ice shelf topography
722 on frazil-laden Ice Shelf Water plumes. *J. Phys. Oceanogr.*, 36, 2312-2327.
- 723 Holland, D. M., and A. Jenkins (1999), Modeling thermodynamic ice-ocean interactions
724 at the base of an ice shelf. *J. of Phys. Oceanogr.* 29.8, 1787-1800.
- 725 Hellmer H.H., Olbers D. J. (1989), A two-dimensional model for the thermohaline circu-
726 lation under an ice shelf. *Antarctic Science*, 1, 325- 336.
- 727 Hopkins, M. A. (1996). On the mesoscale interaction of lead ice and floes. *J. of Geophys.*
728 *Res.: Oceans*, 101(C8), 18315-18326.
- 729 Jakobsen, T. (2001). Advanced character physics. In *Game Developers Conference*, Vol.
730 3.

- 731 Jenkins, A., P. Dutrieux, S. S. Jacobs, S. D. McPhail, J. R. Perrett, A. T. Webb, and
732 D. White (2010), Observations beneath Pine Island Glacier in West Antarctica and
733 implications for its retreat. *it Nature Geo.*, 3(7), 468-472.
- 734 Jacobs, S. S., A. Jenkins, C. F. Giulivi, and P. Dutrieux (2011). Stronger ocean circulation
735 and increased melting under Pine Island Glacier ice shelf. *Nature Geo.*, 4(8), 519-523.
- 736 Jongma, J. I., E. Driesschaert, T. Fichefet, H. Goosse, and H. Renssen (2009), The effect of
737 dynamic-thermodynamic icebergs on the Southern Ocean climate in a three-dimensional
738 model, *Ocean Modell.*, 26, 104113.
- 739 Lewis E.L. and R.G. Perkin (1986), Ice pumps and their rates. *J. of Geophys. Res.*, 91,
740 11756-11762.
- 741 Losch, M. (2008). Modeling ice shelf cavities in az coordinate ocean general circulation
742 model. *J. of Geophys. Res.: Oceans*, 113(C8).
- 743 Li, B., H. Li, Y. Liu, A. Wang and S. Ji (2014), A modified discrete element model for
744 sea ice dynamics. *Acta Oceanologica Sinica*, 33(1), 56-63.
- 745 Liu, M. B. and G. R. Liu (2010), Smoothed particle hydrodynamics (SPH): an overview
746 and recent developments. *Archives of computational methods in engineering*, 17(1), 25-
747 76.
- 748 Lichy, C., and H. H. Hellmer (2001). Modeling giant-iceberg drift under the influence of
749 sea ice in the Weddell Sea, Antarctica. *J. of Glaciol.*, 47(158), 452-460.
- 750 Levermann, A., T. Albrecht, R. Winkelmann, M. A. Martin, M. Haseloff, and I. Joughin.
751 (2012), Kinematic first-order calving law implies potential for abrupt ice-shelf retreat.
752 *The Cryosphere*, 6(2), 273-286.

- 753 Martin, T., and Adcroft, A. (2010), Parameterizing the fresh-water flux from land ice
754 to ocean with interactive icebergs in a coupled climate model. *Ocean Modelling*, 34(3),
755 111-124.
- 756 Marsh, R., V. O. Ivchenko, N. Skliris, S. Alderson, G. R. Bigg, G. Madec, A. T. Blaker
757 Y. Aksenov, B. Sinha, A.C. Coward, and J.L. Sommer (2015), NEMOICB (v1. 0):
758 interactive icebergs in the NEMO ocean model globally configured at eddy-permitting
759 resolution. *Geoscientific Model Development* 8, no. 5 (2015): 1547-1562.
- 760 MacAyeal D.R. (1984), Thermohaline Circulation Below the Ross Ice Shelf: A Conse-
761 quence of Tidally Induced Vertical Mixing and Basal Melting. *J. Geophys. Res.*, 89,
762 597-606
- 763 Nicholls K.W. (1996), Temperature variability beneath Ronne Ice Shelf, Antarctica, from
764 thermistor cables. *J. Phys. Oceanogr.*, 11, 1199-1210.
- 765 Nicholls KW, Østerhus S, Makinson K (2009), Ice-Ocean processes over the continental
766 shelf of the southern Weddell Sea, Antarctica: a review. *Rev. Geophys.* 47(3).
- 767 Omelyan, I. P., M. I. Mryglod, and R. Folk (2002), Optimized Verlet-like algorithms for
768 molecular dynamics simulations. *Physical Review E*, 65(5), 056706.
- 769 Rignot, E., S. Jacobs, J. Mouginot, and B. Scheuchl (2013), Ice-shelf melting around
770 Antarctica. *Science*, 341, no. 6143 (2013): 266-270.
- 771 Robinson, N. J., M. J. M. Williams, P. J. Barrett, and A. R. Pyne (2010), Observations of
772 flow and ice-ocean interaction beneath the McMurdo Ice Shelf, Antarctica, *J. Geophys.
773 Res.*, 115, C03025
- 774 Pan, W., A. M. Tartakovsky, and J. J. Monaghan (2013). Smoothed particle hydrody-
775 namics non-Newtonian model for ice-sheet and ice-shelf dynamics. *J. of Comp. Phys.*,

- 776 242, 828-842.
- 777 Pralong, A., and M. Funk (2005), Dynamic damage model of crevasse opening and appli-
778 cation to glacier calving, *J. Geophys. Res.*, 110, B01309.
- 779 Sergienko, O. V. (2013). Basal channels on ice shelves. *J. of Geophys. Res.: Earth Surface*,
780 118(3), 1342-1355.
- 781 Silva, T. A. M., Bigg, G. R., and Nicholls, K. W. (2006), Contribution of giant icebergs
782 to the Southern Ocean freshwater flux. *J. of Geophys. Res.: Oceans*, 111(C3).
- 783 Smith, K., B. Robison, J. Helly, R. Kaufmann, H. Ruhl, H., T. Shaw, and M. Vernet
784 (2007), Free-drifting icebergs: Hotspots of chemical and biological enrichment in the
785 Weddell Sea, *Science*, 317, 478482.
- 786 Stern, A. A., D. M. Holland, P. R. Holland, A. Jenkins and J. Sommeria (2014), The effect
787 of geometry on ice shelf ocean cavity ventilation: a laboratory experiment. *Experiments*
788 *in Fluids*, 55(5), 1-19.
- 789 Stern, A.A., Johnson, E., Holland, D.M., Wagner, T.J., Wadhams, P., Bates, R., Abra-
790 hamsen, E.P., Nicholls, K.W., Crawford, A., Gagnon, J. and Tremblay, J.E. (2015),
791 Wind-driven upwelling around grounded tabular icebergs. *J. of Geophys. Res.: Oceans*,
792 120(8), 5820-5835.
- 793 Stern, A. A., A. Adcroft, and O. Sergienko (2016), The effects of Antarctic iceberg calv-
794 ing?size distribution in a global climate model. *J. of Geophys. Res.: Oceans*, 121(8),
795 5773-5788.
- 796 Swope, W. C., H. C. Andersen, P. H. Berens, and K. R. Wilson (1982), A computer
797 simulation method for the calculation of equilibrium constants for the formation of
798 physical clusters of molecules: Application to small water clusters. *The Journal of*

- 799 *Chemical Physics* 76, no. 1, 637-649.
- 800 Tournadre, J., N. Bouhier, F. Girard-Ardhuin, and F. Rmy (2016), Antarctic icebergs
- 801 distributions 1992-2014. *J. Geophys Res: Oceans*.
- 802 Vernet, M., et al. (2012), Islands of ice: Influence of free-drifting Antarctic icebergs on
- 803 pelagic marine ecosystems, *Oceanography*, 25(3), 3839
- 804 Weeks, W. F., and W. J. Campbell (1973). Icebergs as a fresh-water source: an appraisal.
- 805 *J. of Glaciol.*, 12(65), 207-233.

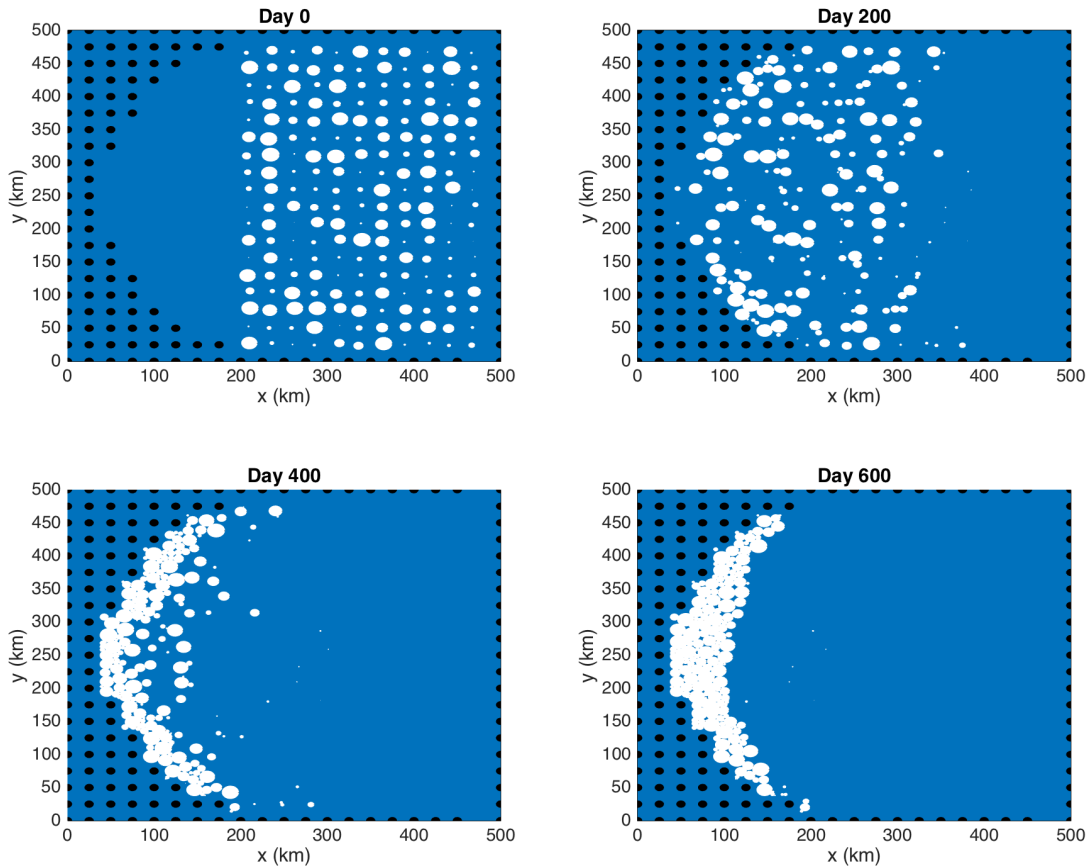


Figure 1. Positions of ice elements at time $t=0, 200, 400, 600$ days for the simulation. The size of the dots shows the surface area (and interaction diameter) of each ice element. Land points are shown by black circles.

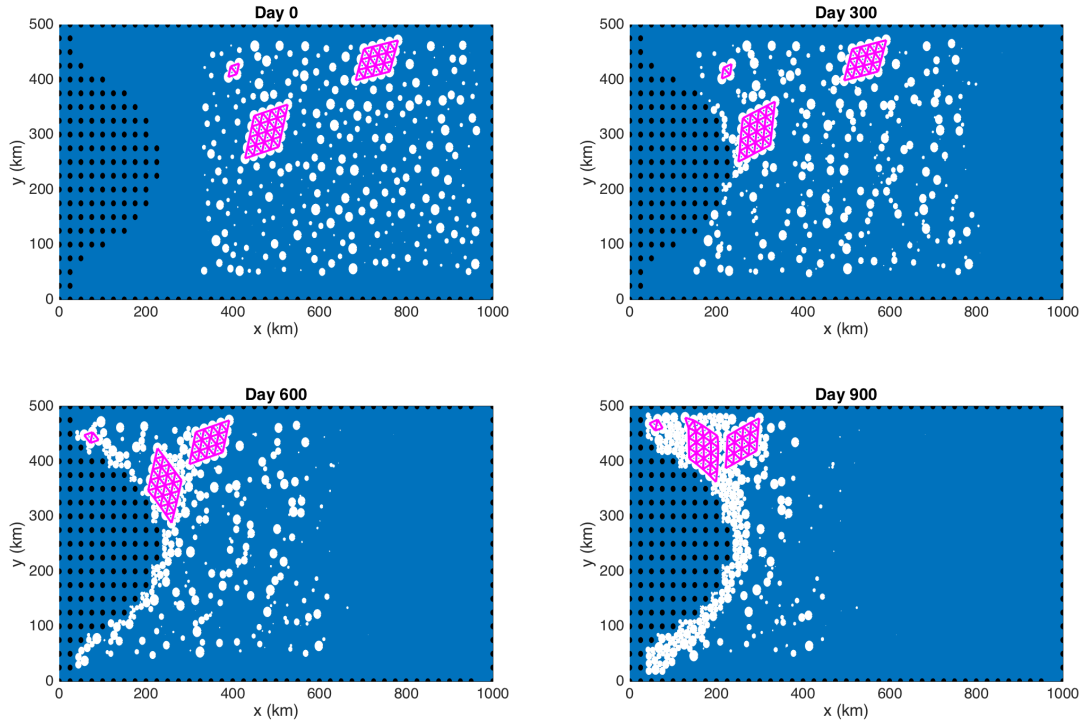


Figure 2. Positions of ice elements at time $t=0, 300, 600, 900$ days for the simulation. The size of the dots shows the surface area (and interaction diameter) of each ice element. Bonds between ice elements are plotted in magenta. Three tabular icebergs are shown, with 25, 16 and 4 elements respectively. Land points are shown by black circles.

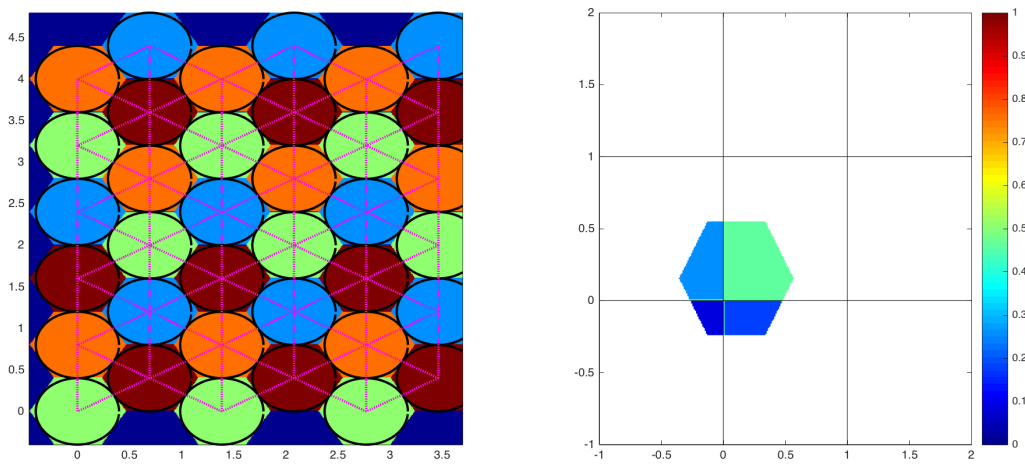


Figure 3. (a) Intersection of hexagonal element and ocean grid is used to find weights to spread LIISM properties to the ocean grid. (b) Hexagonal elements are initialized in a staggered lattice as shown. Adjacent elements are bonded together. The centers of bonded elements are plotted in pink. The element bonds form equilateral triangles which give the larger structure rigidity. The black circles shows to the interactive length scales used in element interactions.

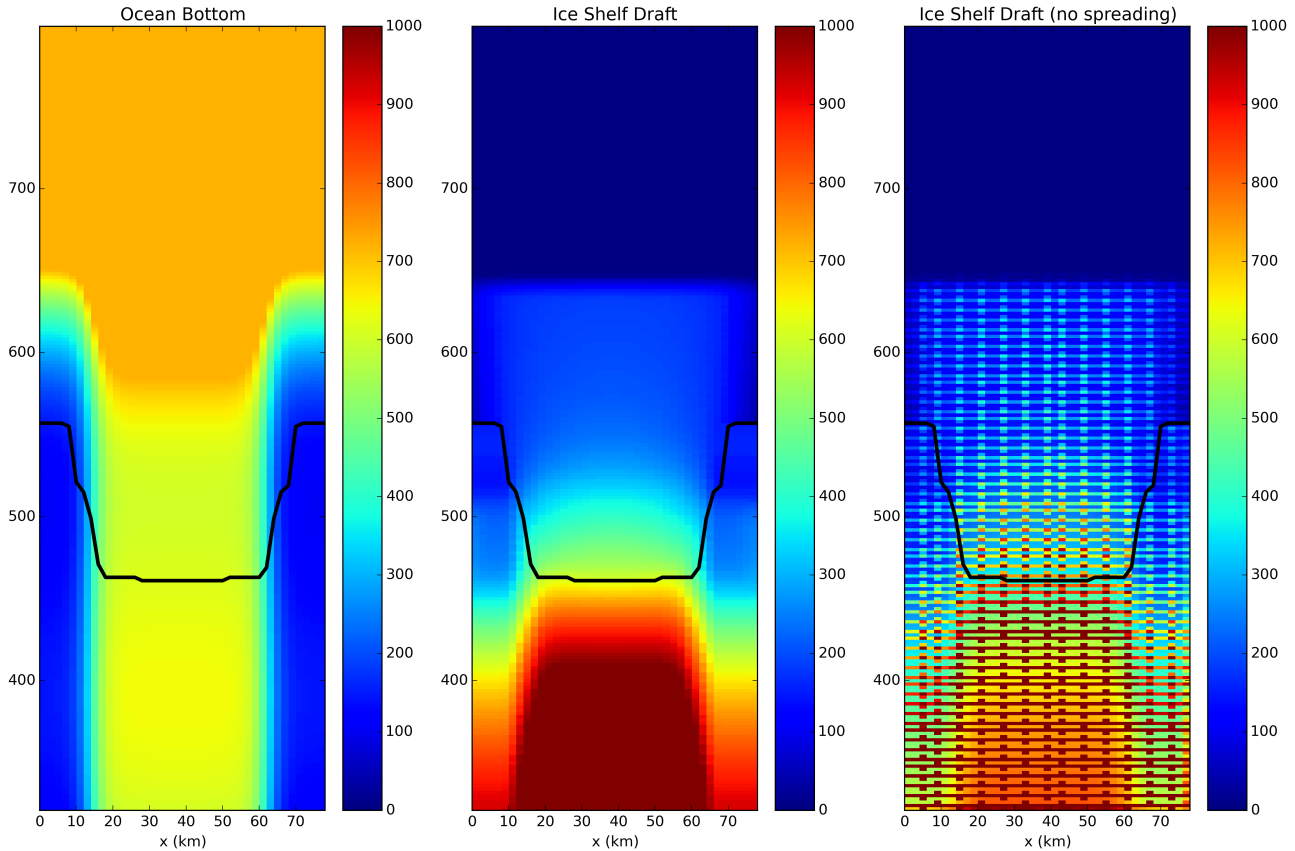


Figure 4. (a) Ocean bottom topography in ISOMIP configuration. (b) Ice shelf draft used in static shelf experiment. The ice draft is calculated from the ice mass in an ocean grid cell, which is found by spreading ice mass across ocean cells accounting for the size of each element (as explained in Section 2.3). (c) Same as in panel (b), except that the interpolation does not account for iceberg size, and instead treats elements as point masses.

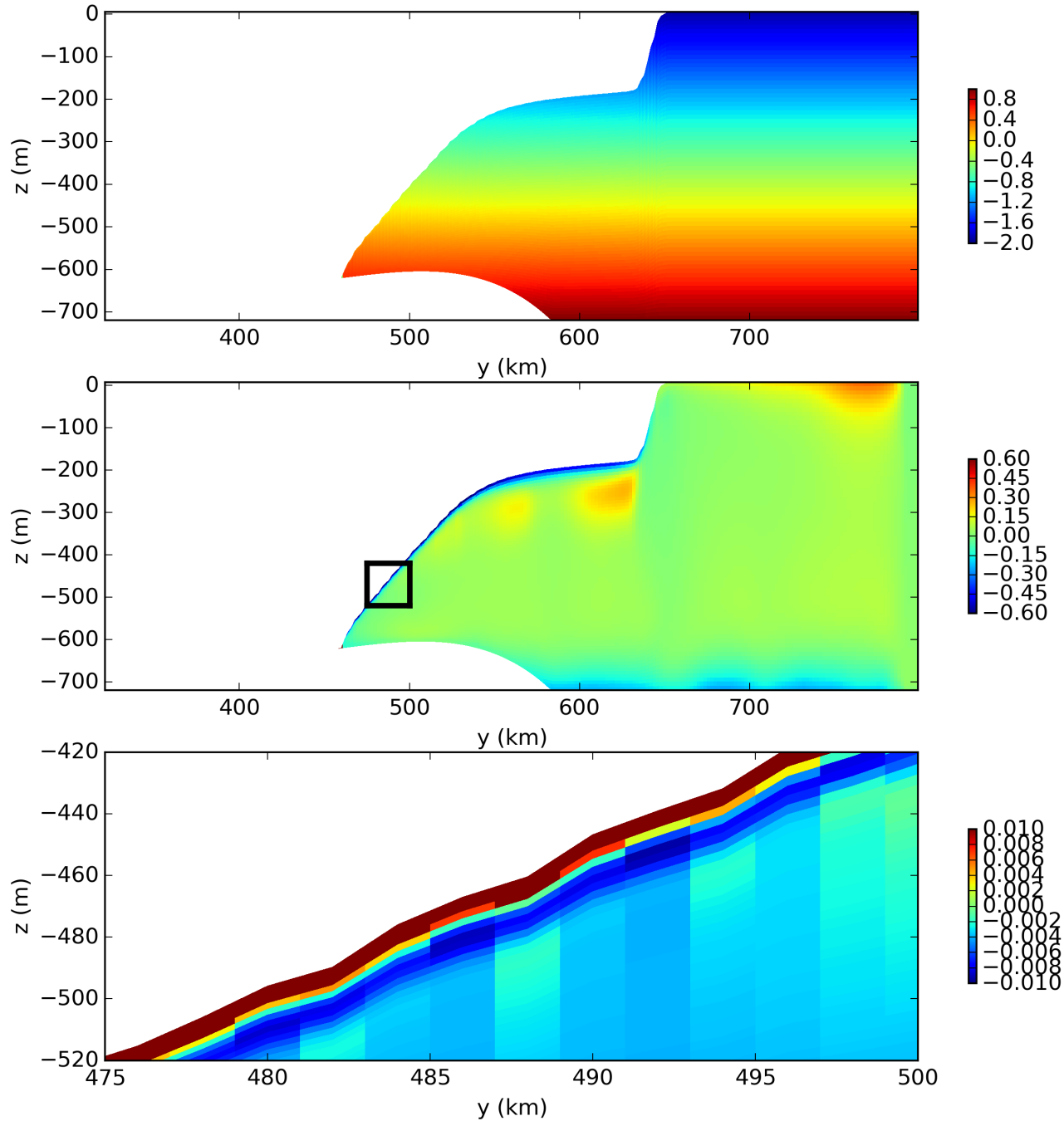


Figure 5. Results of the static ice shelf experiment using the LIISM model. Panels show a cross section of the (a) initial temperature field, (b) temperature anomaly after 5-years (relative to the initial field), and (c) meridional velocity after 5 years of simulation.

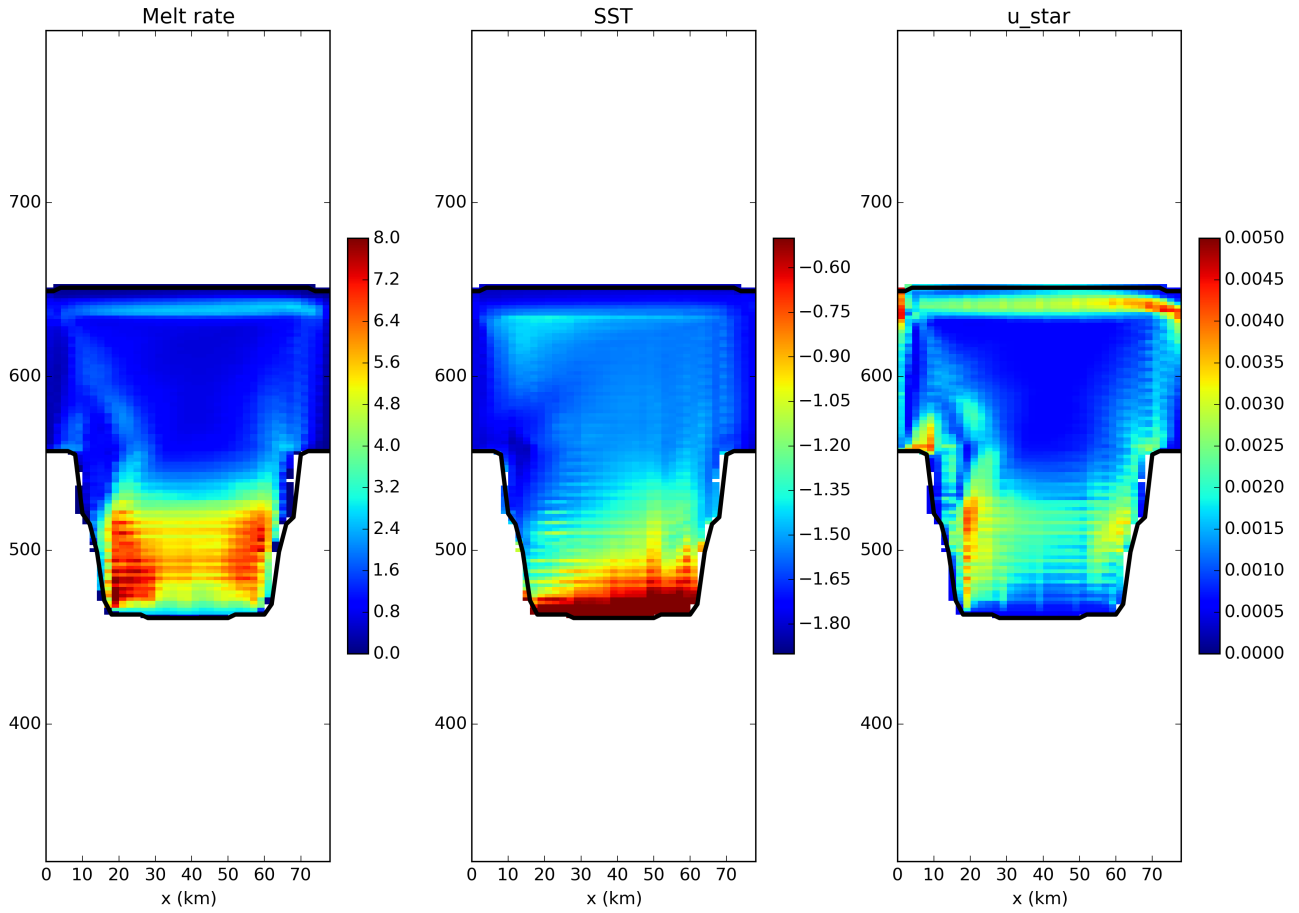


Figure 6. Results of the static ice shelf experiment using the LIISM model. The three panels show 5 year time average of the (a) melt rate, (b) ocean surface temperature and (c) u^* in the top layer of the simulation at the base of the ice shelf.

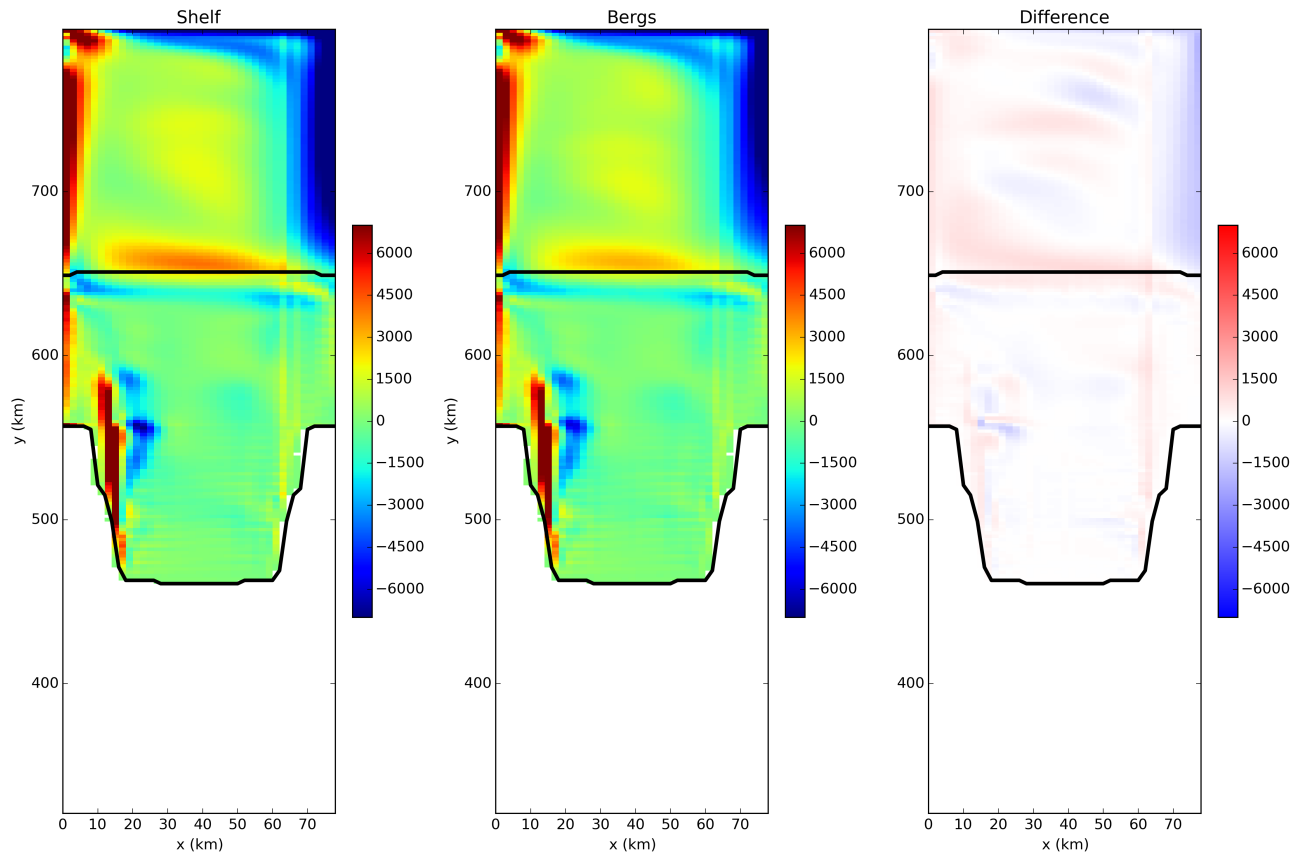


Figure 7. ALE Comparison of Eulerian ice shelf model and Lagrangian Ice shelf model barotropic stream function

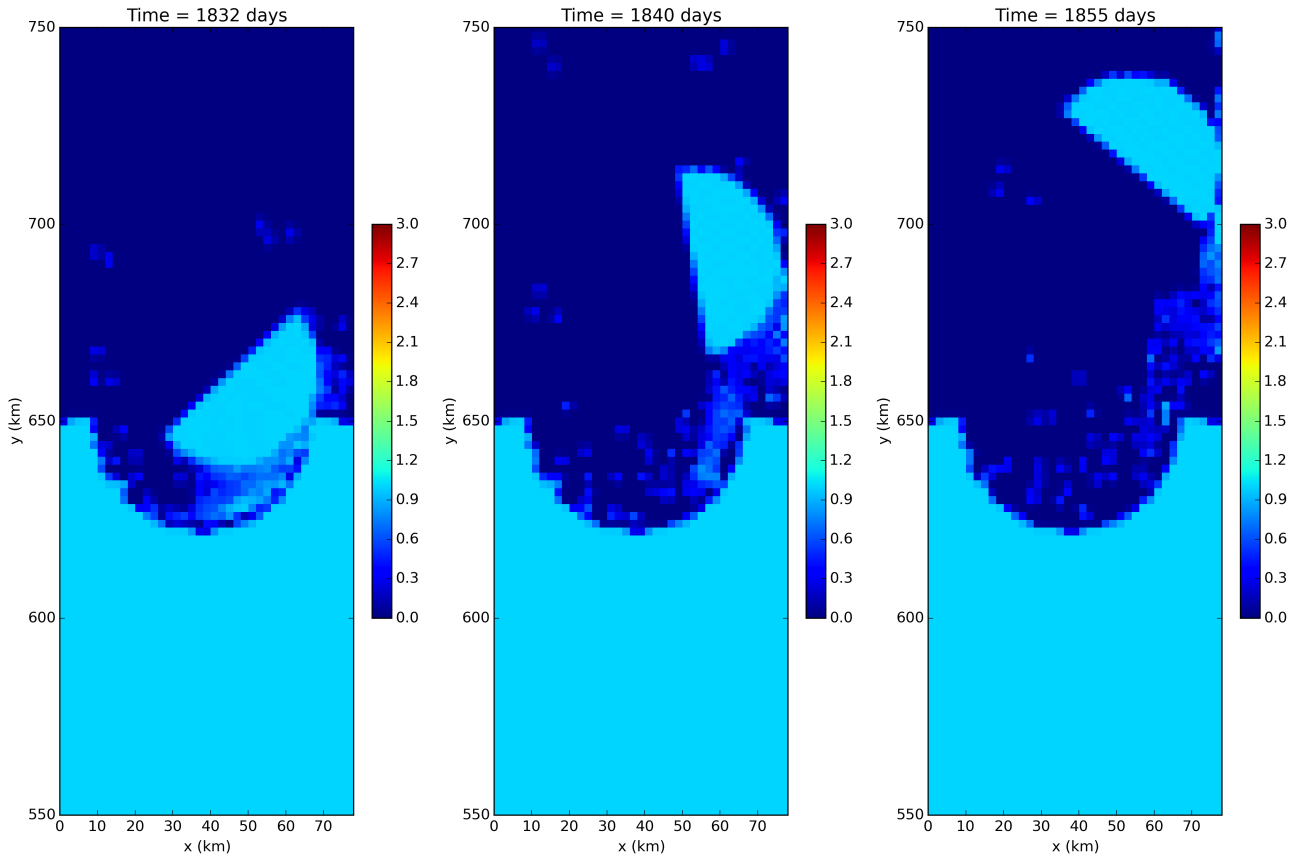


Figure 8. Fraction of grid cell covered by ice (using the LIISM ice shelf) (a) $t=15$, (b) $t=30$, and (c) $t=60$ days after calving.

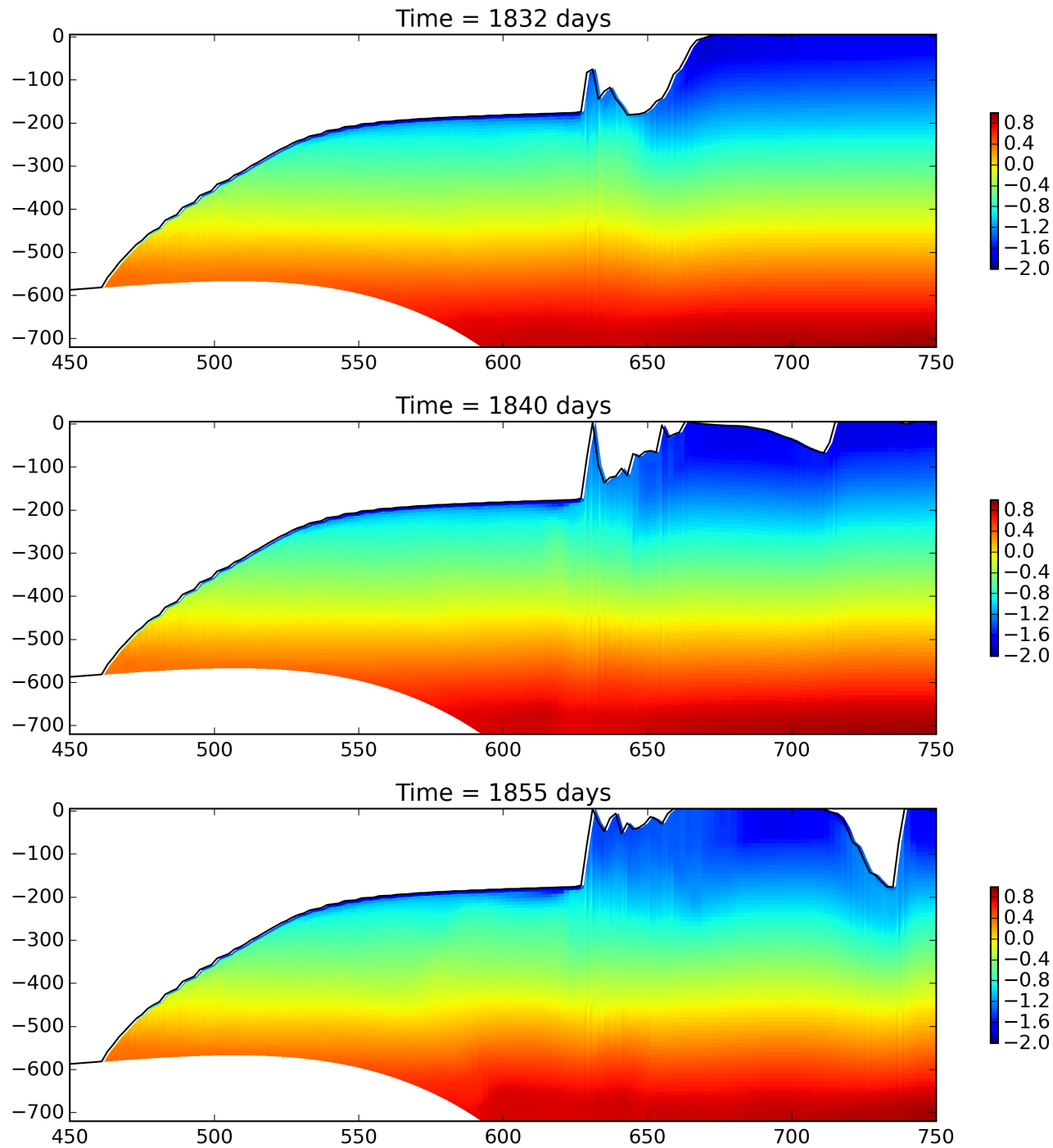


Figure 9. Temperature section at $x = 70\text{ km}$ for the tabular iceberg calving simulation (a) $t=15$, (b) $t=30$, and (c) $t=60$ days after calving.

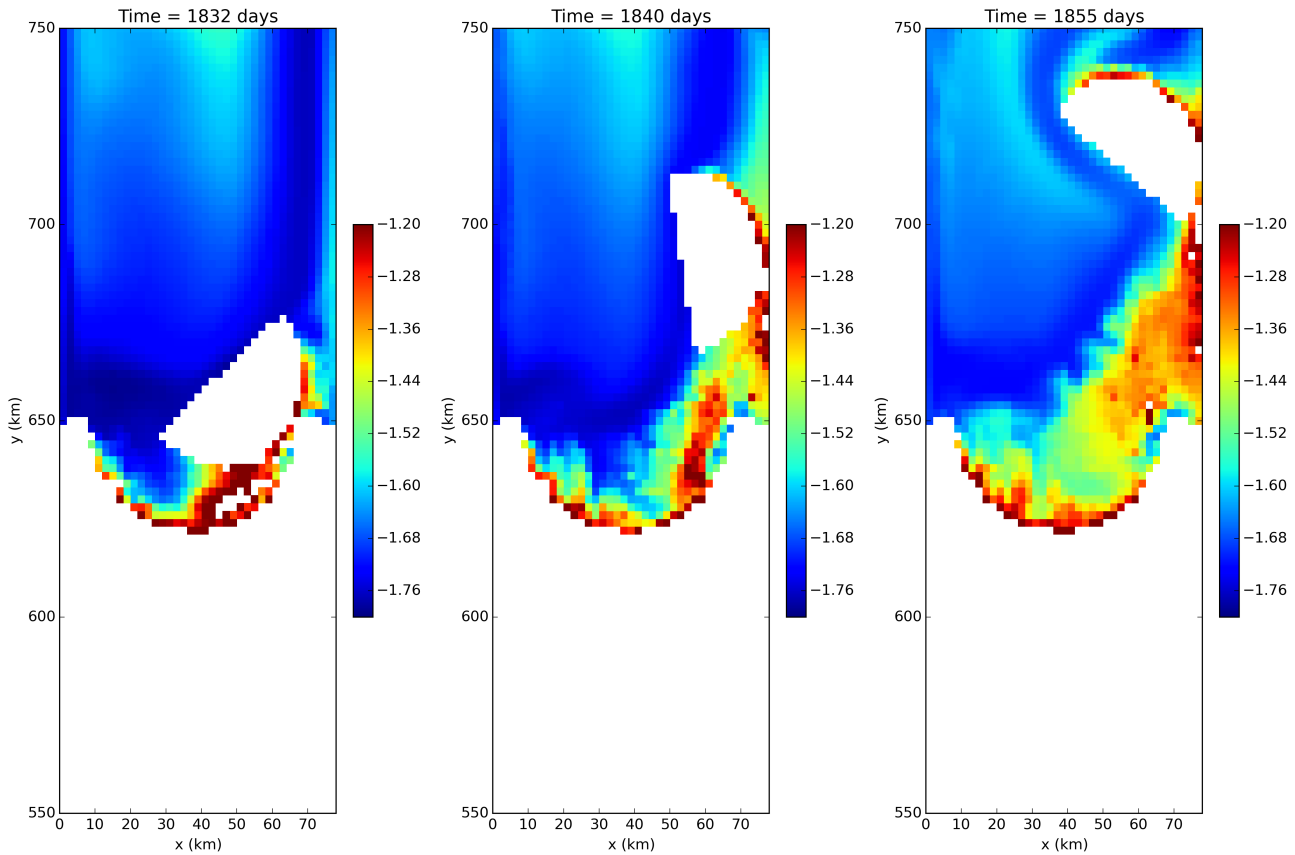


Figure 10. Sea surface temperature for the tabular iceberg calving simulation (a) $t=15$, (b) $t=30$, and (c) $t=60$ days after calving. Regions with ice area fraction = 1 area plotted in white.

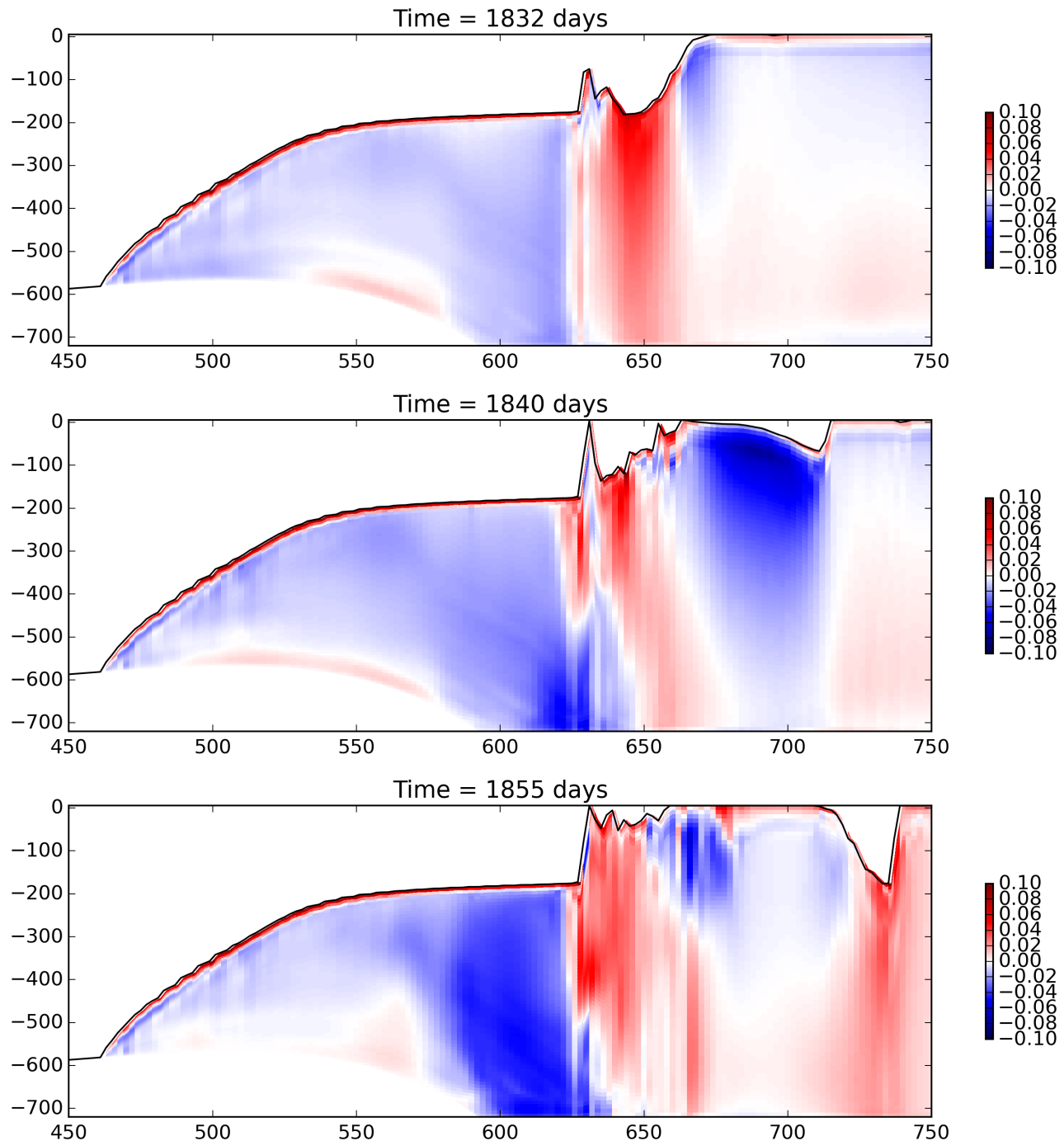


Figure 11. Meridional velocity section at $x = 70\text{ km}$ for the tabular iceberg calving simulation
(a) $t=15$, (b) $t=30$, and (c) $t=60$ days after calving.

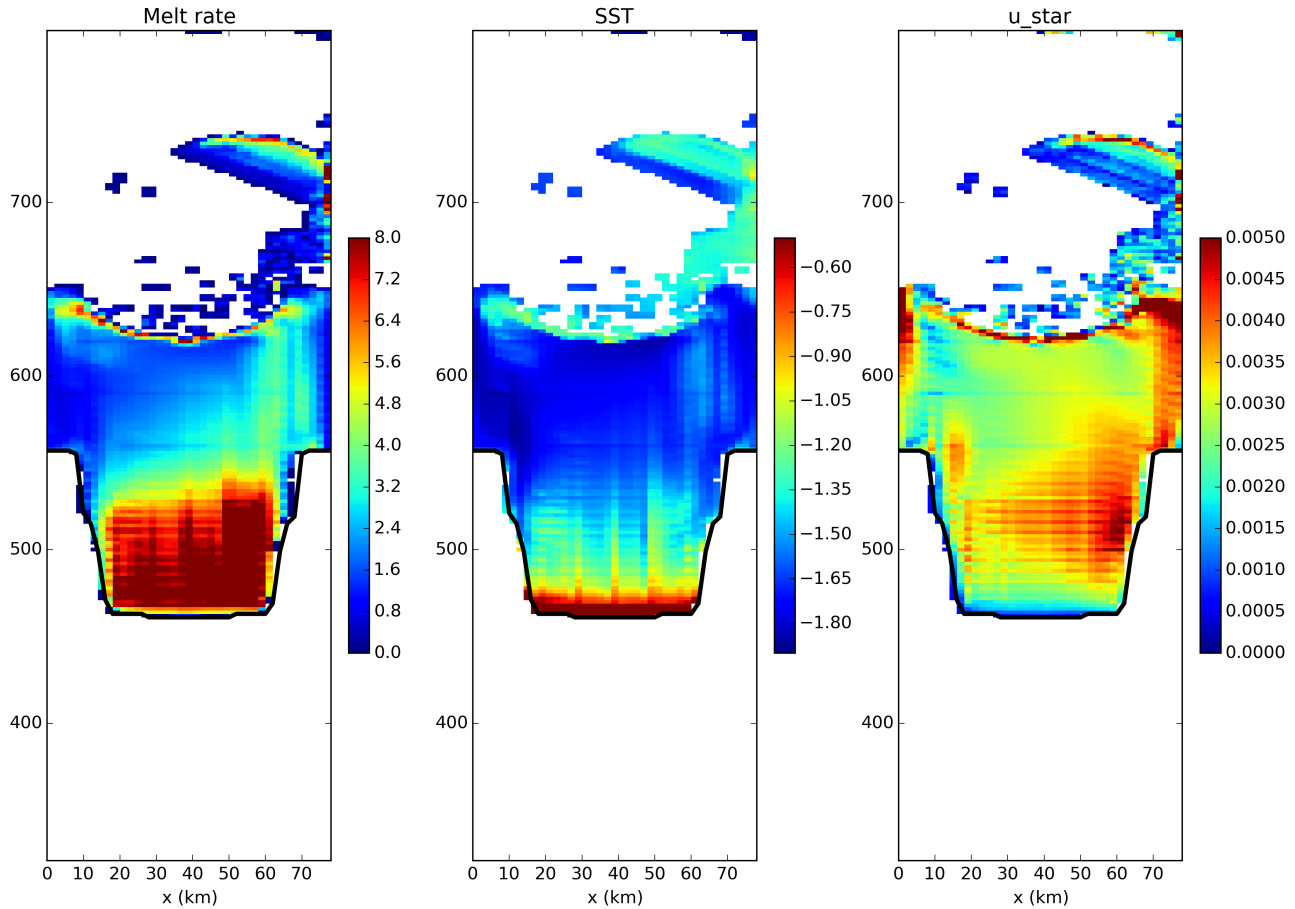


Figure 12. Results of the tabular iceberg calving simulation 60 days after the iceberg calves.

The three panels show 5 year time average of the (a) melt rate, (b) ocean surface temperature and (c) u^* at the base of the ice shelf. Fields are only shown in regions where the ice area fraction is ≥ 0.8 .

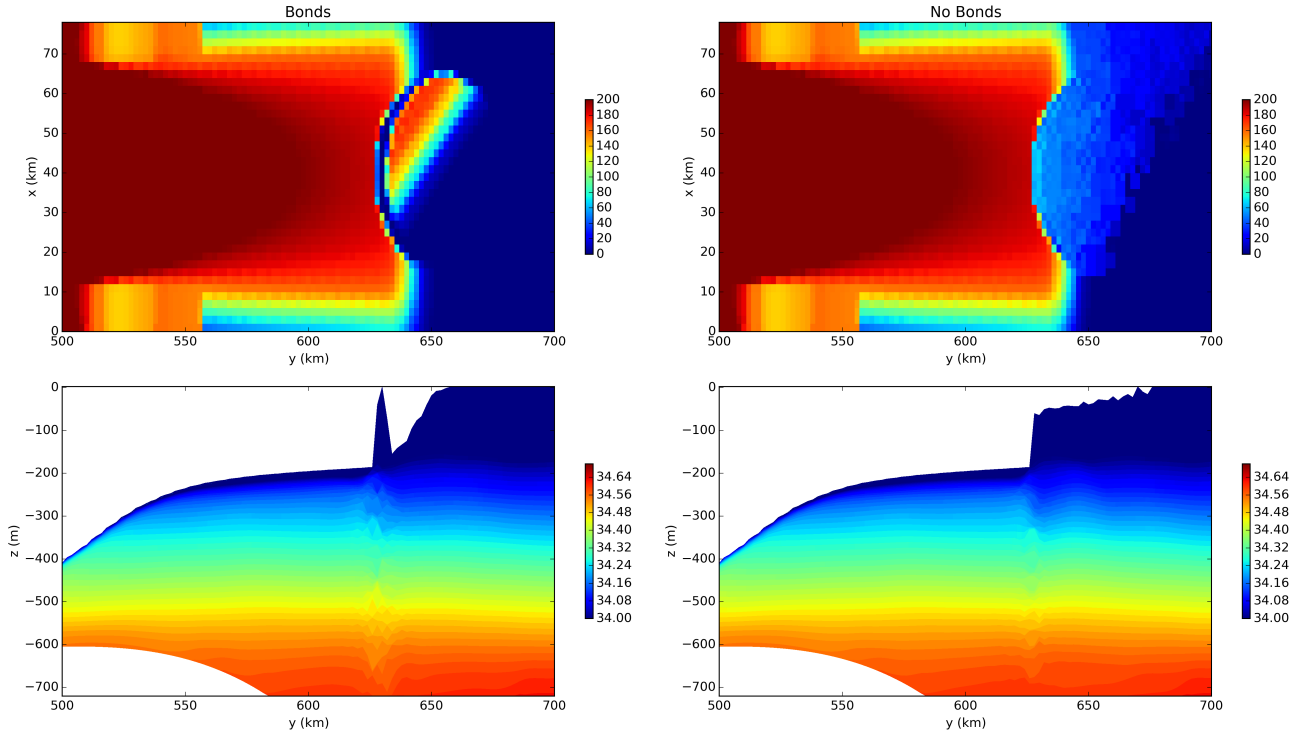


Figure 13. Calving of tabular iceberg with the LIISM model fully coupled to the ocean for simulations with and without bonds between ice elements. The top row show the aveage draft of ice above the ocean in each grid cell for the simulation (a) with and (b) without bonds. The bottom row shows the corresponding temperature section at $y = \frac{L_y}{2}$ for the simulation (a) with and (b) without bonds. All snapshots are taken at time $t = 30$ days.

10. Supplementary Figures

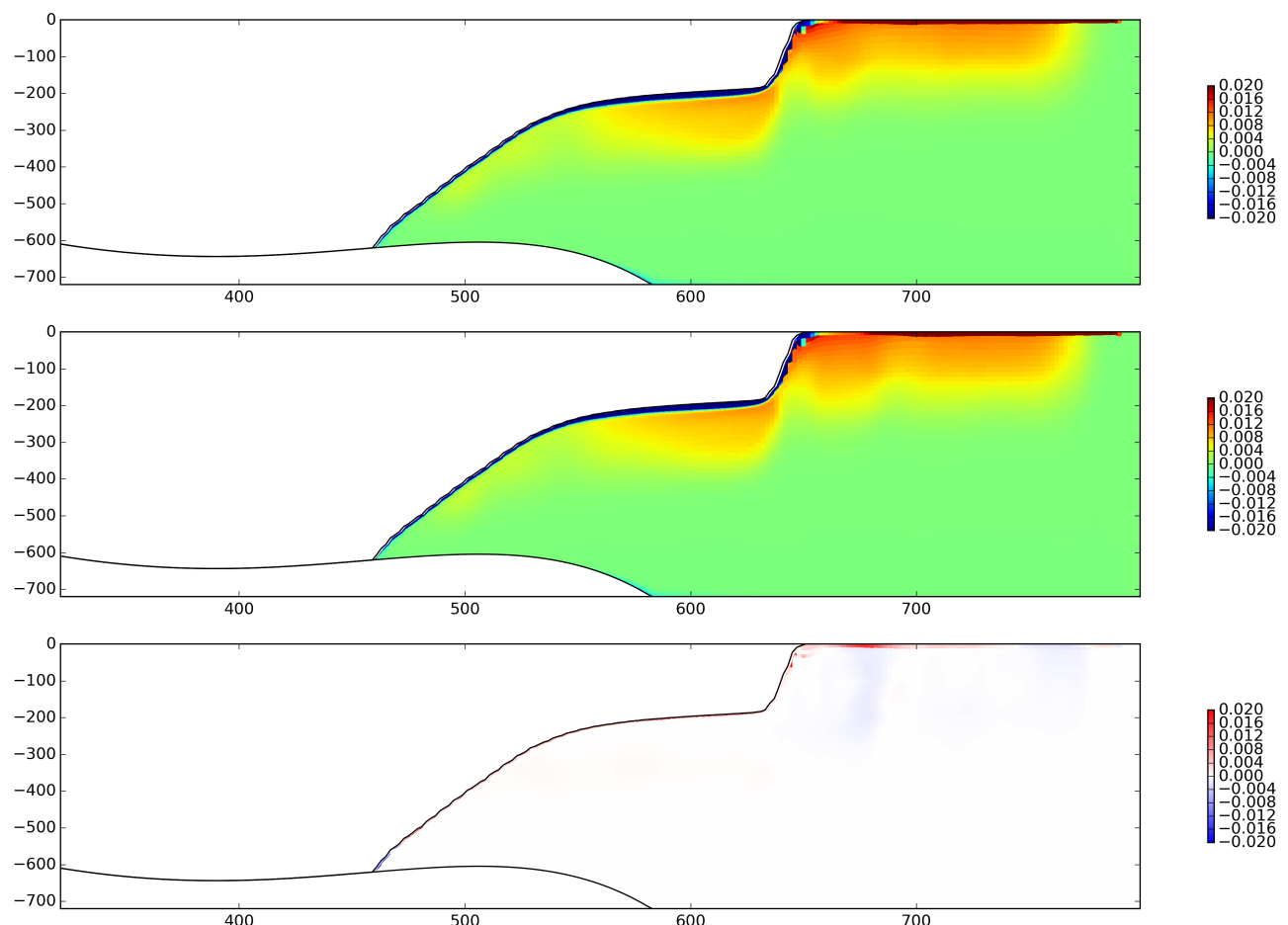


Figure S1. Comparison of Eulerian ice shelf model and Lagrangian Ice shelf model salinity fields.

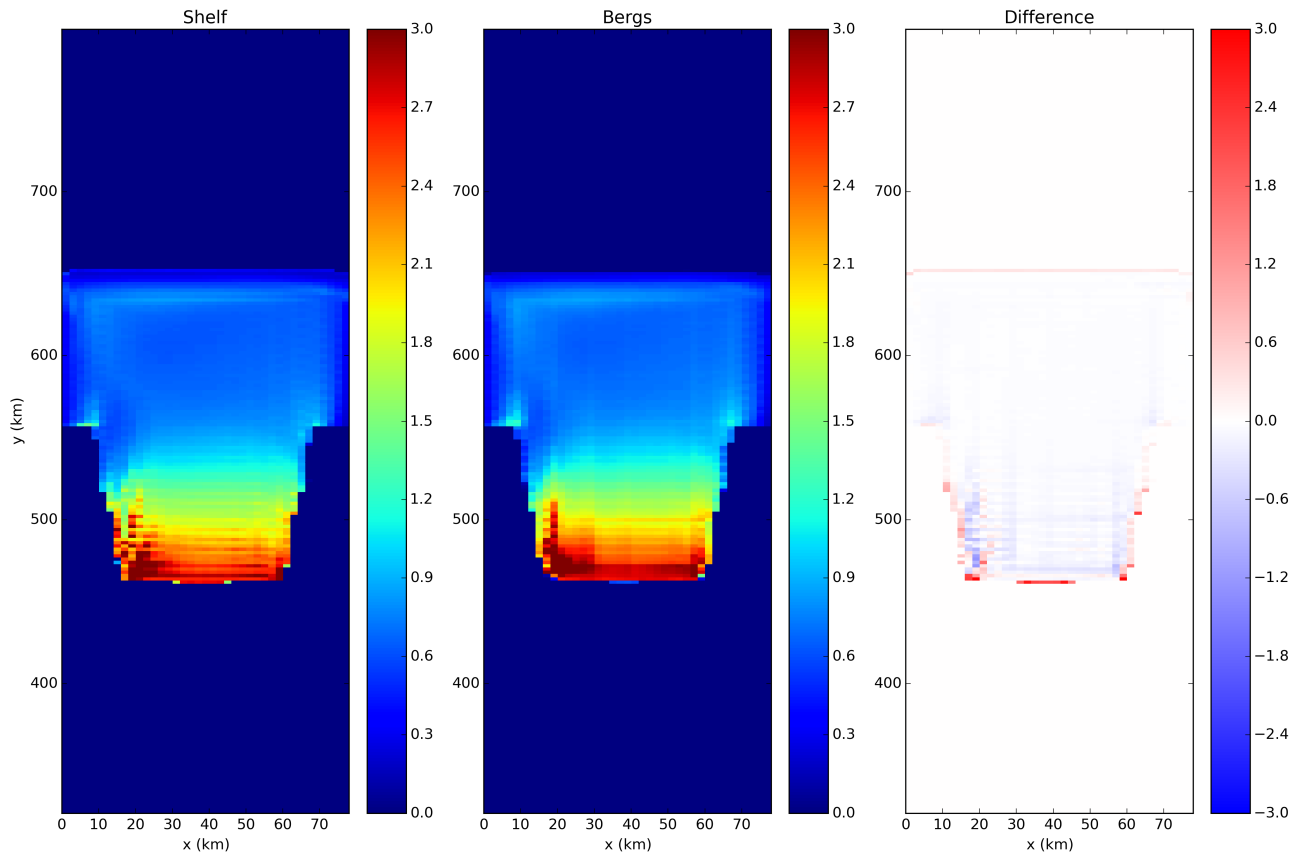


Figure S2. Comparison of Eulerian ice shelf model and Lagrangian Ice shelf model melt fields.

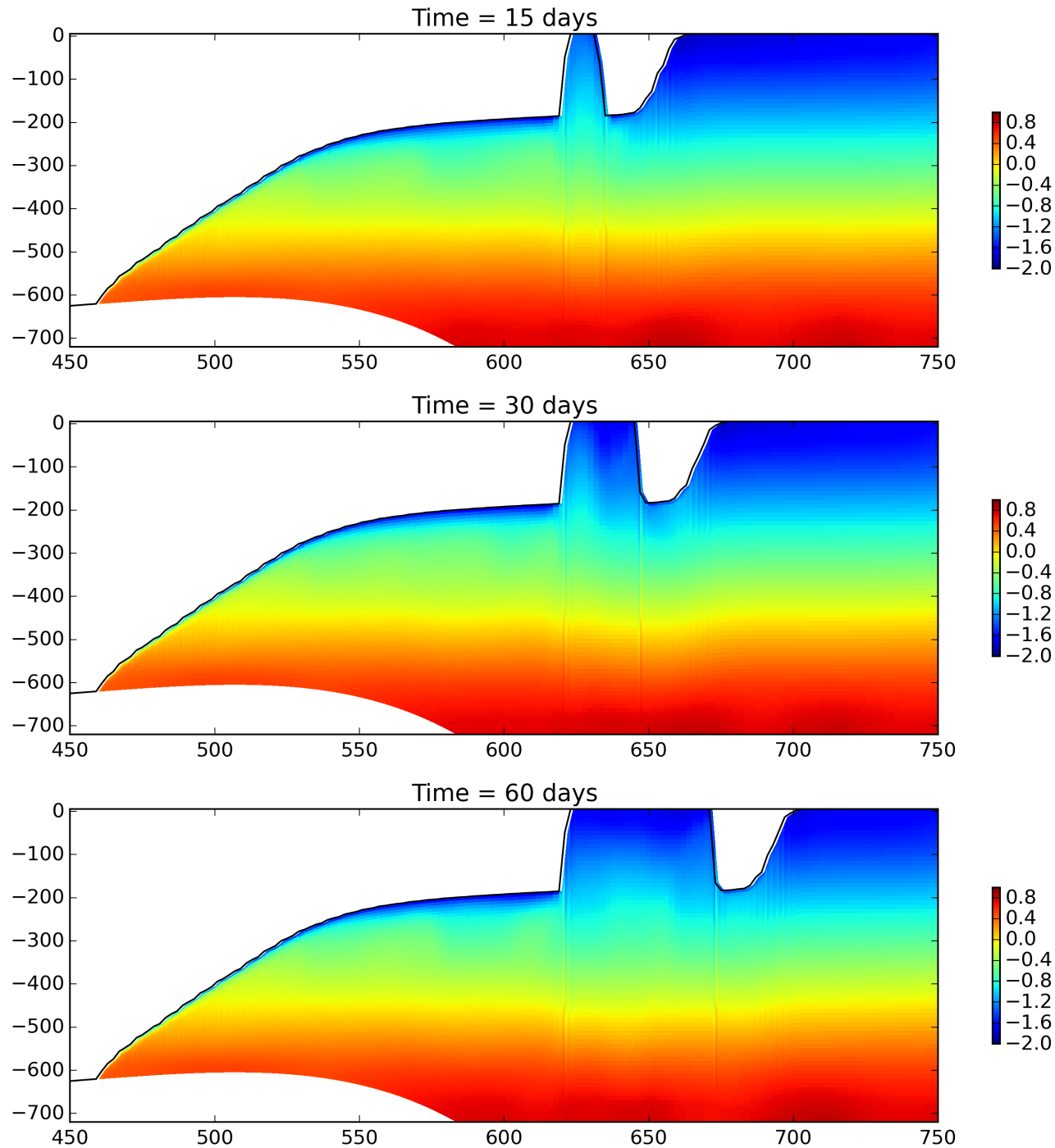


Figure S3. Layer: Temperature section at $y = \frac{L_y}{2}$ for the tabular iceberg calving with fixed velocity simulation (using the LIISM ice shelf) at time (a) $t=15$, (b) $t=30$, and (c) $t=60$ days.

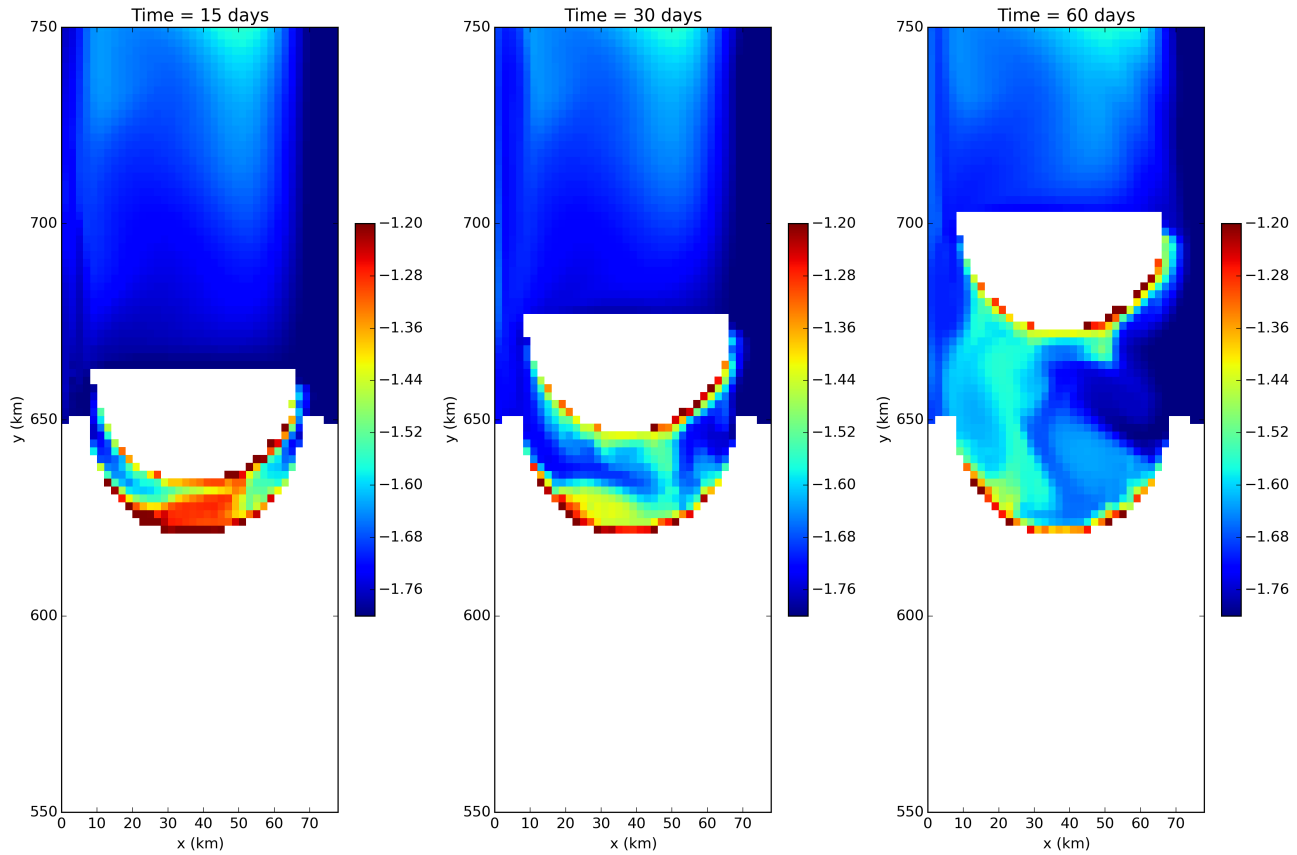


Figure S4. Layer: Sea surface temperature for the tabular iceberg calving with fixed velocity simulation at time (a) $t=15$, (b) $t=30$, and (c) $t=60$ days.

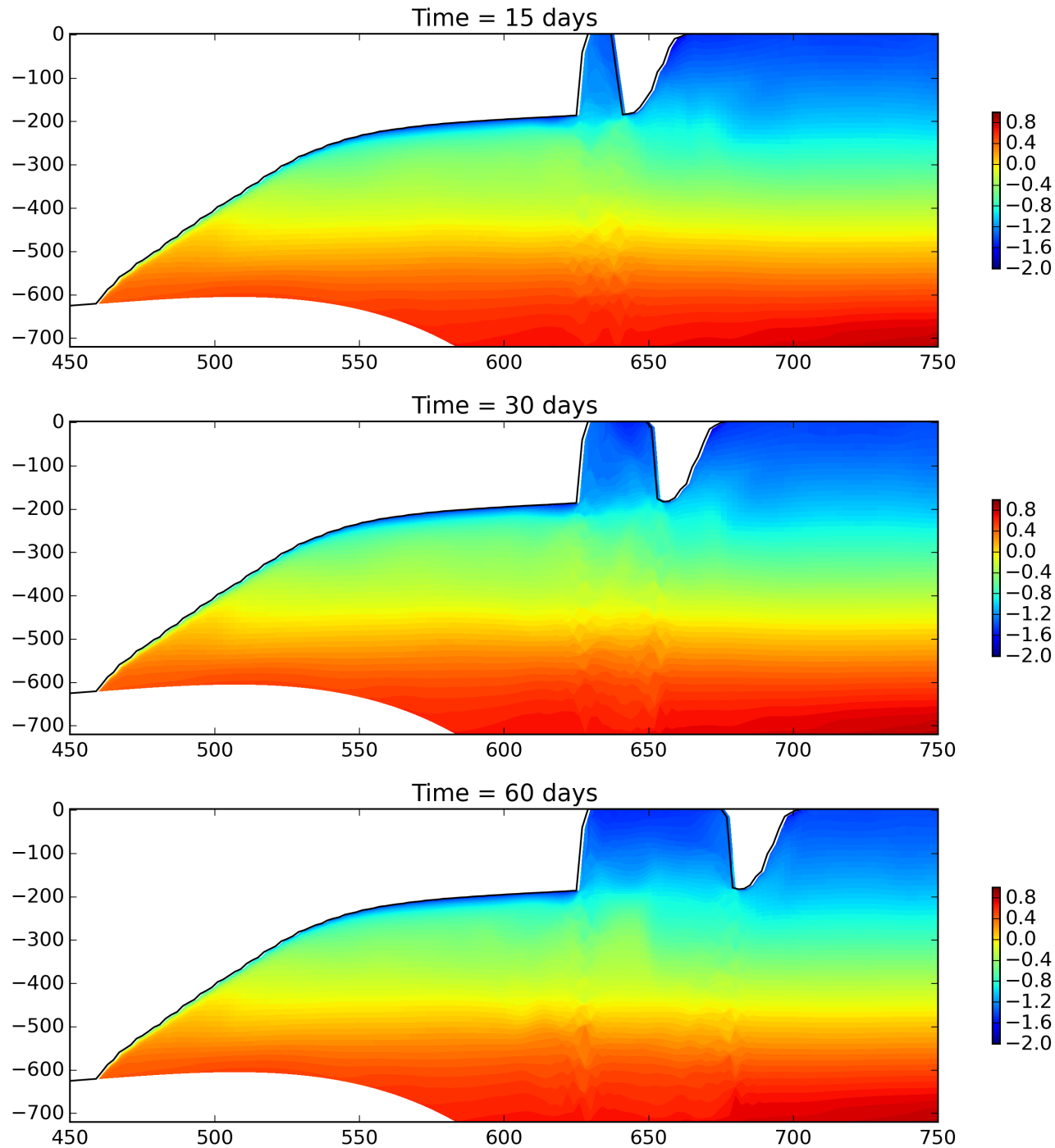


Figure S5. Layer: Temperature section at $y = \frac{L_y}{2}$ for the tabular iceberg calving with fixed velocity simulation (using the LIISM ice shelf) at time (a) $t=15$, (b) $t=30$, and (c) $t=60$ days.

11. Layer versions

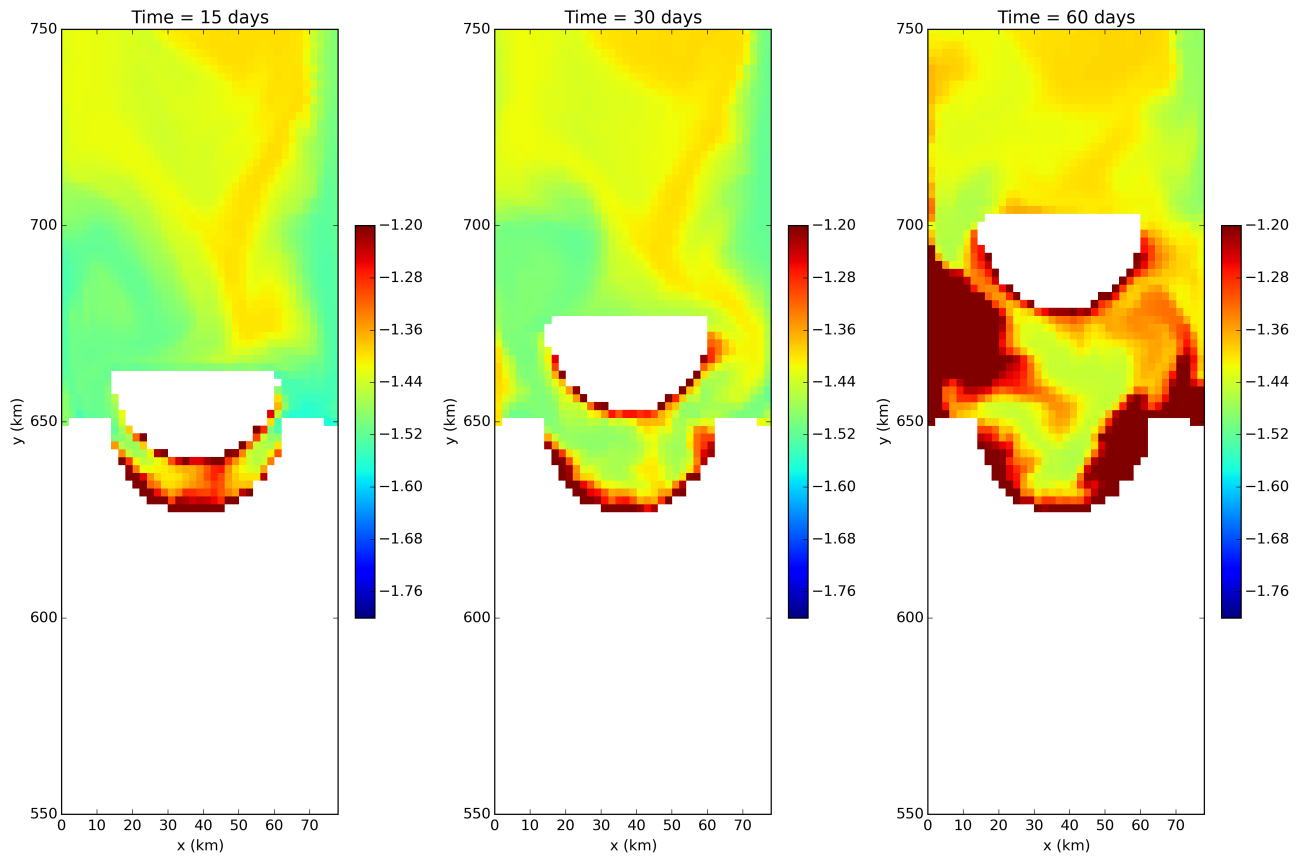


Figure S6. Layer: Sea surface temperature for the tabular iceberg calving with fixed velocity simulation at time (a) $t=15$, (b) $t=30$, and (c) $t=60$ days.

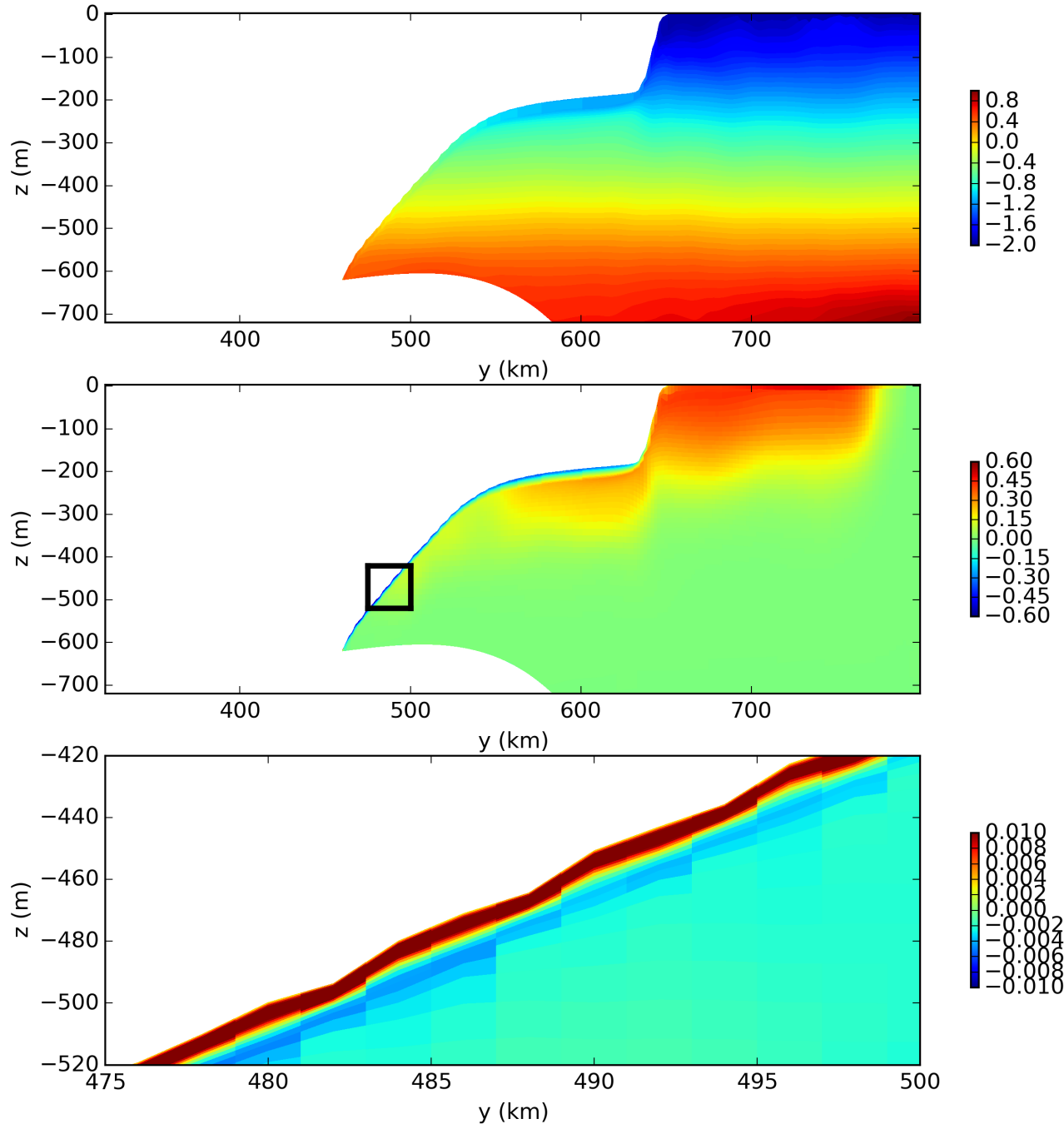


Figure S7. Layered: Results of the static ice shelf experiment using the LIISM model. Panels show snapshots of cross sections of the (a) temperature field after 1 time step, (b) temperature anomaly after 5-years (relative to the initial field), and (c) meridional velocity after 5 years.

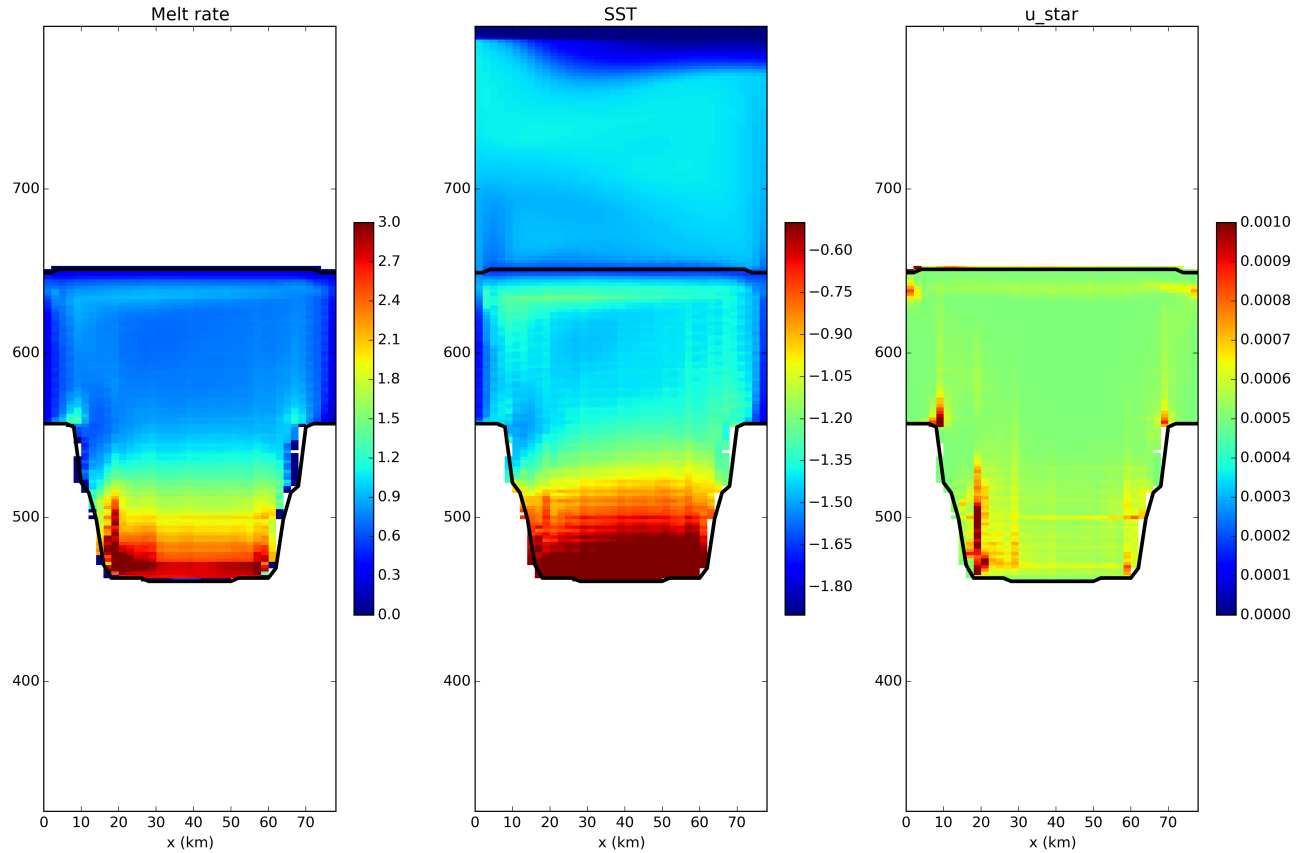


Figure S8. Layer: Results of the static ice shelf experiment using the LIISM model. The three panels show 5 year time average of the (a) melt rate, (b) ocean surface temperature and (c) u^* in the top layer of the simulation (at the surface or directly below the ice shelf).

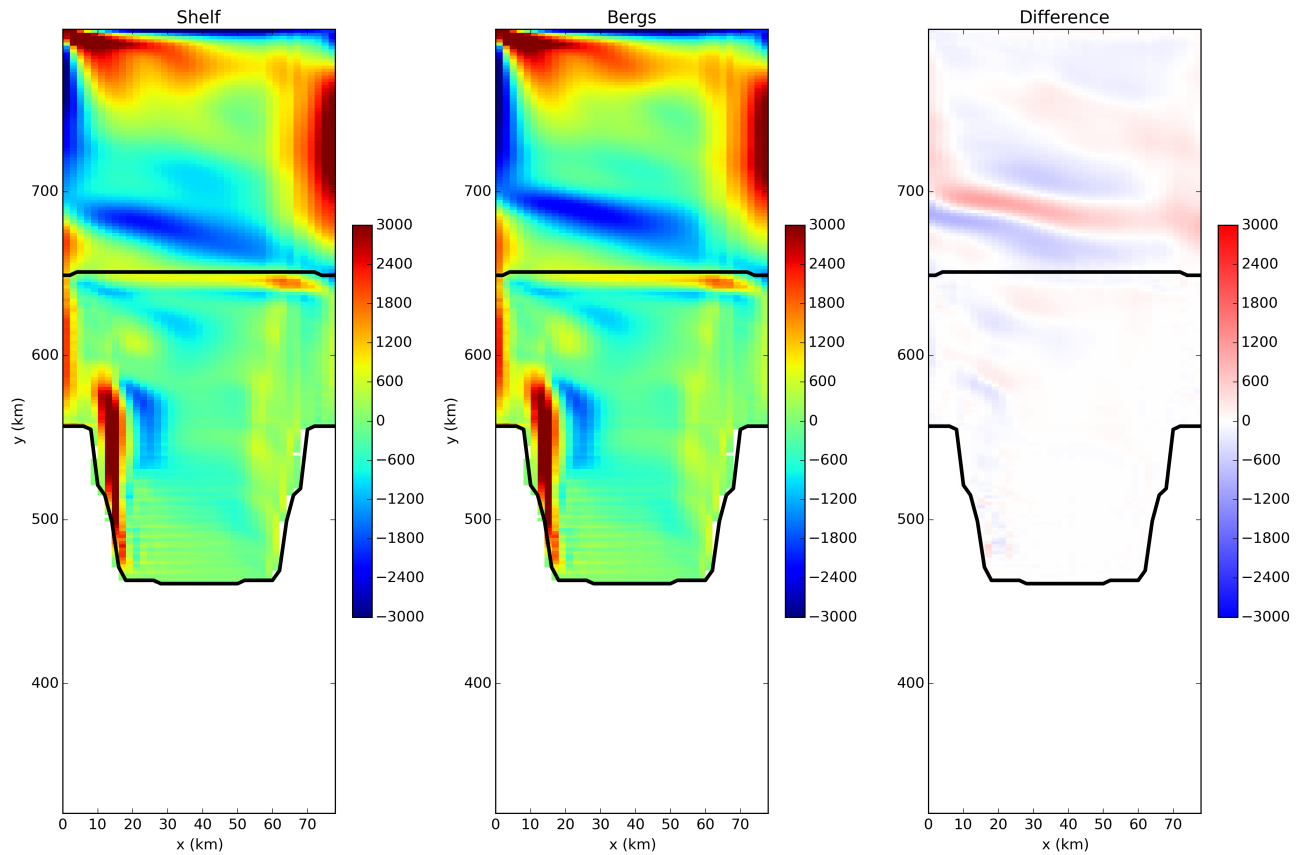


Figure S9. Layer: Comparison of Eulerian ice shelf model and Lagrangian Ice shelf model barotropic stream function